ORIGINAL ARTICLE

Targeting PKM2 signaling cascade with salvianic acid A normalizes tumor blood vessels to facilitate chemotherapeutic drug delivery

Cheng Qian[a,†], Yueke Zhou[a,†], Teng Zhang[a], Guanglu Dong[b], Mengyao Song[a], Yu Tang[a], Zhonghong Wei[a], Suyun Yu[b], Qiuhong Shen[b], Wenxing Chen[a], Jaesung P. Choi[c], Juming Yan[d], Chongjin Zhong[b], Li Wan[e], Jia Li[f], Aiyun Wang[a,*], Yin Lu[a,*], Yang Zhao[a,b,*]

[a]Jiangsu Key Laboratory for Pharmacology and Safety Evaluation of Chinese Materia Medica, Nanjing University of Chinese Medicine, Nanjing 210023, China
[b]School of Medicine & Holistic Integrative Medicine, Nanjing University of Chinese Medicine, Nanjing 210023, China
[c]Centre for Inflammation, Faculty of Science, Centenary Institute, School of Life Sciences, University of Technology Sydney, Sydney NSW 2050, Australia
[d]Jiangsu Key Laboratory of Immunity and Metabolism, Department of Pathogenic Biology and Immunology, National Experimental Demonstration Center for Basic Medicine Education, Xuzhou Laboratory of Infection and Immunity, Xuzhou Medical University, Xuzhou 221004, China
[e]Department of General Surgery, Jiangsu Province Hospital of Chinese Medicine, Affiliated Hospital of Nanjing University of Chinese Medicine, Nanjing 210029, China
[f]Macquarie Medical School, Faculty of Medicine, Human Health Sciences, Macquarie University, Sydney NSW 2109, Australia

Abstract Aberrant tumor blood vessels are prone to propel the malignant progression of tumors, and targeting abnormal metabolism of tumor endothelial cells emerges as a promising option to achieve vascular normalization and antagonize tumor progression. Herein, we demonstrated that salvianic acid A (SAA) played a pivotal role in contributing to vascular normalization in the tumor-bearing mice,

*Corresponding author.

   E-mail addresses: y.zhao@njucm.edu.cn (Yang Zhao), luyingreen@njucm.edu.cn (Yin Lu), wangaiyun@njucm.edu.cn (Aiyun Wang).

†These authors made equal contributions to this work.

thereby improving delivery and effectiveness of the chemotherapeutic agent. SAA was capable of inhibiting glycolysis and strengthening endothelial junctions in the human umbilical vein endothelial cells (HUVECs) exposed to hypoxia. Mechanistically, SAA was inclined to directly bind to the glycolytic enzyme PKM2, leading to a dramatic decrease in endothelial glycolysis. More importantly, SAA improved the endothelial integrity *via* activating the β-Catenin/Claudin-5 signaling axis in a PKM2-dependent manner. Our findings suggest that SAA may serve as a potent agent for inducing tumor vascular normalization.

1. Introduction

It has been widely appreciated that blood vessels are mainly lined with endothelial cells (ECs) and stabilized by recruiting mural cells (pericytes and smooth muscle cells) as well as by deposition of the extracellular matrix, with the function of transporting substances in normal tissues[1,2]. However, blood vessels in tumor tissues are characterized by heterogeneous organization, structure and function, as evidenced by that they exhibit a chaotic, tortuous and incomplete appearance with poor mural cell coverage and abnormal basement membrane support, as well as leaky, poor perfused and immature phenotypes[3,4]. Aberrant tumor blood vessels are inclined to produce a hostile tumor microenvironment (TME) featuring hypoxia, acidity and increased interstitial fluid pressure to set up key hurdles for the delivery of chemotherapeutic agents and penetration of cytotoxic T cells into tumor parenchyma, thereby aggravating tumor progression and inducing therapeutic resistance[5,6]. Vascular normalization, emerging as a promising therapeutic strategy to reverse the structural and functional abnormalities of tumor blood vessels, can be exploited to result in enhanced transport and efficacy of anti-tumor treatments[7,8]. To this end, identifying effective and efficient approaches to achieve tumor vascular normalization is urgently needed.

A growing body of evidence has highlighted that perturbed endothelial metabolism has a high propensity to provoke dysfunction of ECs and further disturb vascular homeostasis under the circumstances of various pathological conditions, particularly in tumors[9,10]. Of note, it has been increasingly recognized that tumor ECs (TECs) and normal ECs (NECs) harbor strikingly different metabolism-associated gene signatures to exhibit distinct metabolic phenotypes[11,12]. In complicated tumor ecosystems, increased hypoxia tends to trigger TECs to skew the predominant metabolic strategy from mitochondrial respiration towards glycolysis to confer the production of adenosine triphosphate, thereby maintaining the hyperactivated status of TECs in comparison to NECs[13]. More interestingly, emerging evidence has shown that elevated glycolysis of TECs plays a pivotal role in giving rise to abnormalities of tumor blood vessels with impaired endothelial junctions[12,14,15]. Therefore, targeting the aberrant metabolism in particular increased glycolysis of TECs paves the way for restoring the endothelial barrier integrity with enhanced expression levels of adherens junctions (AJ)-related molecules (*e.g.*, VE-cadherin) and tight junctions (TJ)-associated molecules (*e.g.*, Claudin-5), which provides a promising therapeutic strategy to fulfill tumor vascular normalization and reprogram the TME. In this regard, understanding the underlying mechanisms of curbing

the excessive glycolysis in TECs is essential for exploring robust and efficient routes to correct abnormal tumor blood vessels and further potentiate alternative anti-tumor therapies.

The activity of the glycolytic enzyme pyruvate kinase M (PKM) has been validated to govern the fate of glucose-derived carbon. *PKM* gene confers splice variants mainly encoding two isoforms, PKM1 and PKM2, that exert striking effects on determining the final step in glycolysis that is catalyzing the formation of pyruvate from phosphoenolpyruvate (PEP)[16]. In fact, it has been widely held that PKM2 is predominantly expressed in numerous types of cells and tissues, as well as plays a vital role in influencing the development of various diseases resulting from its enzymatic and non-enzymatic properties[17,18]. Noteworthily, PKM2 possesses powerful enzymatic function as a tetramer in the cytoplasm, but tends to serve as a transcriptional coactivator in the nucleus upon dissociation of the tetramer into a dimer with impaired enzymatic activity[19]. It has been reported that, in addition to the pyruvate kinase activity, PKM2 has been receiving extensive attention for its noncanonical activity, by which PKM2 exerts prominent impacts on modulating gene expression as a crucial transcription factor coactivator of hypoxia-inducible factor 1-alpha (HIF-1α) and nuclear factor-erythroid factor 2-related factor 2 (Nrf2) or phosphorylating proteins as a protein kinase[19,20]. Recently, an increasing number of studies have revealed the roles of PKM2 in modulating various physiology phenotypes of vascular ECs, including tight junctions, senescence, and redox homeostasis[21–23]. PKM2 has been shown to be able to translocate into the nucleus and then bind to β-Catenin to yield profound consequences on the growth fate of cells[17]. Since endothelial β-Catenin is known to be an important mediator for maintaining vascular integrity[24], targeting PKM2 signaling cascade may offer a promising therapeutic strategy to manipulate tumor blood vessels.

Natural products have long been a primary source to obtain drugs that are utilized to prevent and treat many types of diseases owing to their pronounced effectiveness and high safety[25,26]. Salvianic acid A (SAA) [3-(3,4-dihydroxyphenyl)-2-hydroxypropanoic acid], a main biologically active ingredient derived from *Salvia miltiorrhiza* Burge., has been documented to demonstrate a variety of pharmacological functions, such as anti-oxidative, anti-inflammatory and anti-cancer properties[27,28]. Nevertheless, whether SAA is capable of eliciting striking impacts on regulating tumor blood vessels still remains ambiguous. In the present study, we elucidate that SAA inhibits the endothelial glycolysis and strengthens the endothelial junctions, thereby inciting tumor vascular normalization. The normalized tumor blood vessels by SAA provide a principal route for the delivery of anti-tumor agent to enhance the

efficacy of chemotherapy. Taken together, our findings reveal that SAA acts as a potent natural PKM2 modulator that may be further optimized to be a therapeutic agent for inducing tumor vascular normalization, opening a window to seek promising options for combination cancer therapy.

2. Materials and methods

2.1. Reagents and antibodies

SAA (HY-N1913) and doxorubicin (DOX, HY-15142) were purchased from MedChemExpress (Monmouth Junction, NJ, USA). CD31 (553370) and VE-cadherin (VE-cad, 555289) primary antibodies were from BD Biosciences (Franklin Lake, USA). Collagen IV (Col IV, ab6586), NG-2 (ab255811), ZO-1 (ab96587) and CD31 (ab222783) primary antibodies were purchased from Abcam Technology (Cambridge, UK). α-SMA (19245), Claudin-5 (49564), β-Catenin (8480), p-β-Catenin (4176), PKM2 (4053), Ki67 (9129) and cleaved caspase3 (Cl-Casp3, 9661) primary antibodies were obtained from Cell Signaling Technology (Beverly, USA). HIF-1α (sc-13515), carbonic anhydrase-9 (CA-9, sc-365900), β-actin (sc-47778), Keap1 (sc-514914), Nrf2 (sc-365949), HO-1 (sc-390991), NQO1 (sc-32793) and Lamin B1 (sc-377000) primary antibodies were purchased from Santa Cruz Biotechnology (CA, USA). Fluorescein isothiocyanate (FITC) conjugated anti-mouse CD31 antibody (160212) was acquired from Biolegend (San Diego, CA, USA). Tetramethylrhodamine isothiocyanate (TRITC) conjugated Phalloidin (40734ES80), peroxidase-conjugated goat anti-mouse IgG (H + L) (33201ES60), and peroxidase-conjugated goat anti-rabbit IgG (H + L) (33101ES60) were from YEASEN (Shanghai, China). Goat anti-rabbit IgG H&L Alexa Fluor 488 (ab150077), goat anti-rabbit IgG H&L Alexa Fluor 594 (ab150080), goat anti-mouse IgG H&L Alexa Fluor 488 (ab150113), goat anti-mouse IgG H&L Alexa Fluor 555 (ab150118), and goat anti-mouse IgG H&L Alexa Fluor 594 (ab150116) antibodies were obtained from Abcam Technology (Cambridge, UK). Goat anti-rabbit IgG H&L Alexa Fluor 555 (A-21430) and chicken anti-rat IgG H&L Alexa Fluor 488 (A-21470) antibodies were purchased from Thermo Fisher Scientific (Waltham, MA, USA).

2.2. Patient samples

The primary human lung tumor tissues were collected with prior consent from Jiangsu Province Official Hospital. Paraffin-embedded human lung carcinoma tissue sections were utilized to perform histopathological assessment and immunofluorescence staining. The histopathological classification and the degree of differentiation of lung tumors were independently scored by an experienced pathologist in a blinded manner. The total RNA from freshly harvested lung tumor tissues was extracted for subsequent quantitative reverse-transcription PCR (qRT-PCR) analysis. The study protocol was approved by the Medical Ethical Committee of Jiangsu Province Official Hospital (permit and approval number: 2022009). Written informed consent was obtained from the patients.

2.3. Cell culture

B16F10 murine melanoma cell line and Lewis lung carcinomas (LLC) cell line were obtained from the American Type Culture Collection. B16F10 and LLC cells were maintained in Dulbecco's modified Eagle's medium supplemented with 10% fetal bovine serum and 100 U/mL penicillin and streptomycin (Corning, NY, USA) at 37 °C in an incubator with 5% CO_2. Human umbilical vein endothelial cells (HUVECs) were isolated and purified from the donated umbilical cords as previously described with minor modification[29], as approved by the Medical Ethical Committee of Jiangsu Province Hospital on Integration of Chinese and Western Medicine (permit and approval number: 2021-LWKY-003). Written informed consent was obtained. HUVECs were passaged with trypsin-ethylenediaminetetraacetic acid and used at low passage numbers between 2 and 5. In the hypoxia experiment, HUVECs were maintained under an atmosphere of 1% O_2 for 12 h in the absence or presence of SAA and then used for further analysis. All cells used in this study were negative for mycoplasma as periodically tested by a mycoplasma detection kit (Beyotime, Shanghai, China).

2.4. Lentiviral transduction

The (ZsGreen-Puro)/U6-PKM2 and (ZsGreen-Puro)/U6-NC lentivirus were purchased from Corues Biotechnology (Nanjing, China). HUVECs were plated into six-well plates and upon reaching approximately 80% confluency transfected with lentivirus-mediated small interference RNA (siRNA) in accordance with the manufacturer's protocol. Briefly, HUVECs were transduced with the lentiviral particles in 2% (v/v) fetal bovine serum medium for 12 h in the presence of 10 μg/mL adjuvant polybrene, after which the medium was removed and replaced by the fresh medium. Following 48 h of transduction, the HUVECs were collected and then the transfection efficiency was evaluated using the qRT-PCR and Western blot assays. The sequences of gene-specific primer sets used in this study are listed in Supporting Information Table S1. The Luciferase-EGFP-IRES-Puro lentivirus was obtained from Genechem Co., Ltd. (Shanghai, China). B16F10 and LLC cells were infected with the lentivirus for 12 h, followed by replacing with fresh medium. The cells were collected for subsequent experiments 72 h after transfection.

2.5. Mouse tumor model and treatment regimens

Male C57BL/6J mice (6−8 weeks old, 20−22 g) were purchased from Shanghai SLAC Laboratory Animal Co., Ltd. (Shanghai, China). All animals were maintained within specific pathogen-free facilities at the Laboratory Animal Center of Nanjing University of Chinese Medicine. All animal protocols were approved by the Animal Care and Use Committee of Nanjing University of Chinese Medicine (permit and approval number: 202105A028) and performed in accordance with the institutional guidelines of Nanjing University of Chinese Medicine.

Murine syngeneic tumor model was established via subcutaneous inoculation of a total of 1×10^6 B16F10 or LLC cells into the right flank of C57BL/6J mice. Tumors were measured in two dimensions with a digital caliper, and tumor volume was calculated on the basis of Eq. (1):

$$\text{Tumor volume} = D \times d^2 \times 0.5 \tag{1}$$

where D refers to the long axis and d represents the short axis. When the average tumor volume reached 100 mm³, saline or 40 mg/kg SAA was intraperitoneally administered into the tumor-bearing mice every day. In light of the assessment of chemotherapeutic drug delivery into tumors, the tumor-bearing mice were treated with saline or SAA daily. Seven days following the

treatment of saline or SAA, 8 mg/kg DOX was intraperitoneally injected into the mice every three days for further 12 days. Upon the termination of DOX treatment, the tumor-bearing mice were sacrificed and the tumors were dissected for further analysis. To investigate the impacts of SAA on normal vascular structure and function, the C57BL/6J mice were injected intraperitoneally with saline or SAA for consecutive 14 days, followed by the examination of normal blood vessels in the lung and liver tissues.

2.6. RNA sequencing (RNA-seq)

In terms of RNA-seq, total RNA was extracted from HUVECs using Trizol reagent (Invitrogen, CA, USA). The integrity of RNA samples was evaluated using the agarose gel electrophoresis and the Agilent 2100 Bioanalyzer (Agilent Technologies). The RNA libraries were sequenced on the Illumina Novaseq 6000 platform by LC-Bio Technology Co., Ltd. (Hangzhou, China). Bioinformatic analysis was carried out on the basis of the R Studio. Significantly differentially expressed genes between vehicle-treated and SAA-treated groups were analyzed by gene set enrichment analysis (GSEA) on the GSEA software (Version 4.0.3), whereby the genes were ranked based on the P values and fold changes.

2.7. Mass spectrometry (MS)-based drug affinity responsive target stability (DARTS) assay

Briefly, HUVECs were lysed with the M-PER mammalian protein extraction reagent (78501, Thermo Fisher Scientific, USA) for 30 min. Subsequently, indicated concentrations of SAA were incubated with the aliquoted cell lysates. In order to enable sufficient binding of SAA and target proteins, the samples underwent mild agitation, followed by a controlled incubation for 2 h at room temperature. The aliquoted lysates were then digested with different ratios of pronase for 30 min, after which the lysates were supplemented with the loading buffer (P0015A, Beyotime, Shanghai, China) and subjected to a 10 min boiling process. The resulting samples were separated using sodium dodecyl sulfate polyacrylamide gel electrophoresis and subsequently subjected to Coomassie blue staining. The protein-containing bands in the gels were excised for in-gel digestion, after which the MS sequencing and data analysis were performed.

2.8. Western blot analysis

Western blot analysis was performed as previously described[28]. Briefly, HUVECs lysates were prepared in appropriate volume of ice-cold radioimmunoprecipitation assay buffer (1 mL per confluent 10^7 cells) containing proteinase and phosphatase inhibitors (Roche, Madison, USA). Total protein concentration was determined using the Pierce BCA Protein Assay Kit as per the manufacturer's instructions (Thermo Fisher Scientific, USA). For non-reducing gradient gel electrophoresis, the protein samples were prepared with the native gel sample loading buffer (P0016N, Beyotime, Shanghai, China). Subsequently, the prepared protein lysates were subjected to polyacrylamide gel electrophoresis and transferred onto polyvinylidene difluoride membranes, which were then blocked in 5% non-fat milk dissolved in TBS-T buffer for 1 h and incubated with the indicated primary antibodies overnight at 4 °C. The polyvinylidene difluoride membranes were further incubated with corresponding secondary antibodies for 1 h

at room temperature, followed by that the blots were developed with the enhanced chemiluminescence reagent (Bio-sharp, Wuhan, China), and the digital images were acquired and densitometry analyses were performed using the Bio-Rad system (Bio-Rad Gel Doc-2000, Hercules, USA).

2.9. Two-photo microscopy imaging

In order to visualize the leakage of tumor blood vessels *in vivo*, LLC tumor-bearing mice were subjected to isoflurane anesthesia after being intravenously administered with 10 mg/kg of 70 kDa TRITC-dextran (25 mg/mL, Sigma−Aldrich, St. Louis, MO, USA). The skin around the tumor was carefully dissected away, followed by that the leakage of tumor blood vessels was monitored in a real-time manner under the 25 × water immersion objective of two-photon confocal microscopy (Olympus FVMPE-RS, Tokyo, Japan).

For investigating the delivery of DOX into tumor parenchyma and assessing tumor vascular perfusion *ex vivo*, 8 mg/kg DOX was intravenously injected into the LLC tumor-bearing mice 1 h prior to euthanasia of mice, and FITC-CD31 was intravenously injected into the tumor-bearing mice 30 min after the injection of DOX. The tumors were harvested and then imaged by using the 25 × water immersion objective of two-photon confocal microscope (Leica STELLARIS 8 DIVE, Heidelberg, Germany).

2.10. Statistical analysis

All data are expressed as mean ± standard deviation (SD), and P value < 0.05 was considered statistically significant, otherwise indicated as nonsignificant (n.s). Animal studies were age-matched and randomized on the basis of body weight. Data determined to be parametric were analyzed using an unpaired Student's t-test (comparing the means of two groups), or ordinary one-way analysis of variance (ANOVA) (comparing differences of means among more than 2 groups). All calculations were performed using GraphPad Prism 8.0 software (San Diego, CA, USA).

3. Results

3.1. SAA delays tumor progression via alleviating hypoxic microenvironment

In order to investigate the pharmacological effects of SAA on tumor progression, two syngeneic murine tumor models characterized by excessive angiogenesis were established *via* subcutaneously implanting LLC and B16F10 tumor cells, and then the tumor-bearing experimental mice received intraperitoneal injection of SAA (40 mg/kg/day) for 14 consecutive days since the tumors became palpable. Intriguingly, it was observed that the relative bioluminescent intensity of tumors treated with SAA was significantly lower than that of treated with vehicle control by virtue of IVIS imaging system (Fig. 1A−D), implying that SAA resulted in remarkable inhibition of tumor growth in comparison to vehicle control. This could be substantiated by the growth curves of tumor volume data, which showed that the mice treated with SAA developed tumors (both LLC and B16F10 tumors) much slower than those treated with vehicle control (Fig. 1E and F). Consistent with the delayed growth rates of tumors by SAA, the average weights of LLC and B16F10 tumors harvested from tumor-bearing mice on the final day of treatments in the SAA-
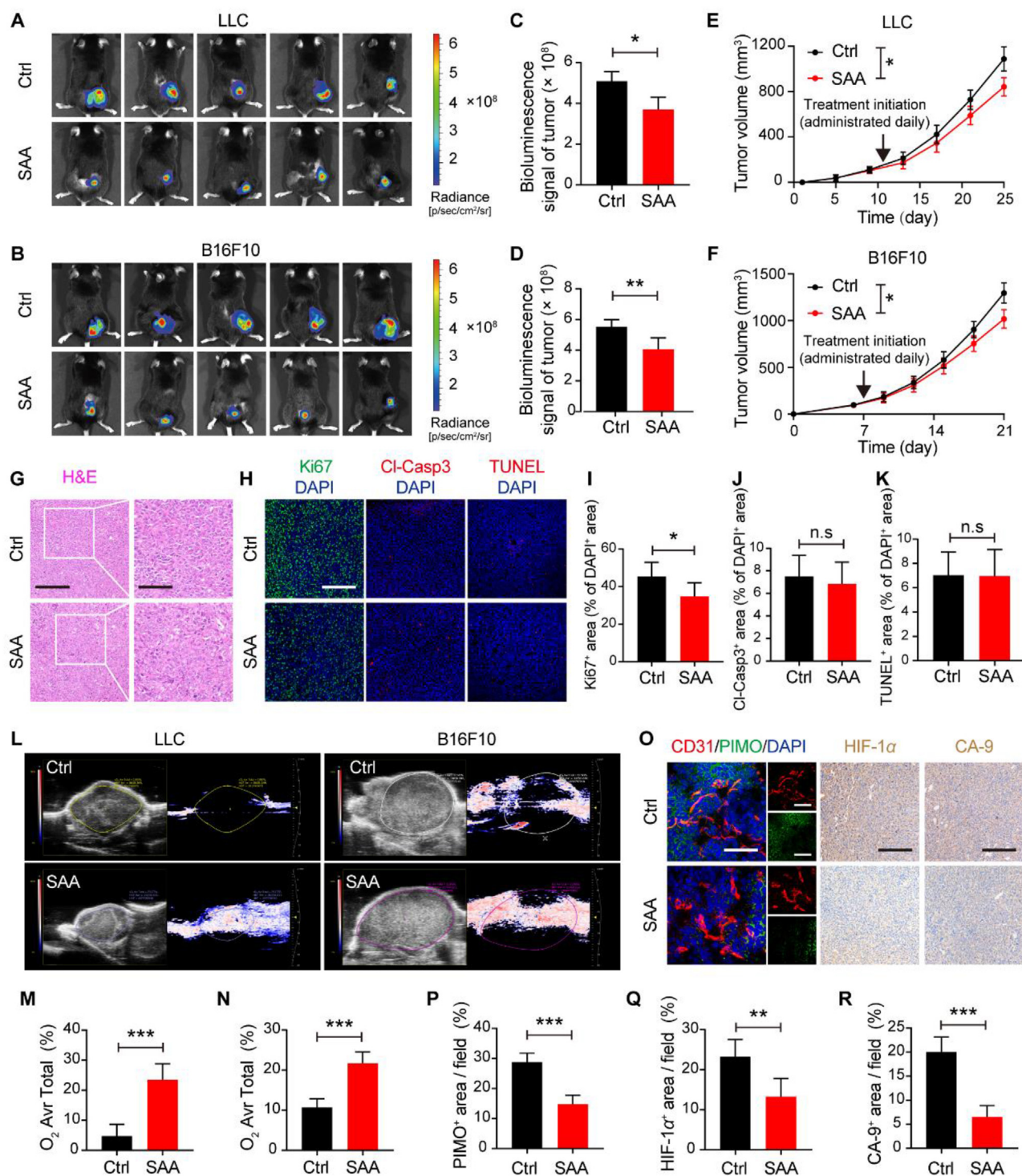
Figure 1 SAA delays tumor progression. (A−D) Bioluminescence images of LLC (A) and B16F10 tumors (B) treated with vehicle Ctrl or SAA (40 mg/kg) and quantification of bioluminescence signals in LLC (C) and B16F10 tumors (D) ($n = 5$). (E, F) The growth curves of LLC (E) and B16F10 tumors (F) for the Ctrl and SAA treated mice ($n = 5$). The LLC tumor-bearing mice were treated daily with saline or SAA from Day 11 following the subcutaneous inoculation of LLC tumor cells. The B16F10 tumor-bearing mice were treated daily with saline or SAA from Day 7 following the subcutaneous inoculation of B16F10 tumor cells. (G) Representative H&E staining images for tumors in the LLC tumor-bearing mice treated with or without SAA. Scale bars: 200 μm; scale bars for zoom in: 100 μm. (H) Representative immunofluorescence staining images for Ki67 (green), Cl-Casp3 (red) and TUNEL (red) with DAPI (blue) in the LLC tumor-bearing mice treated with or without SAA. Scale bars: 200 μm. (I−K) Quantifications for the percentages of Ki67$^+$ (I), Cl-Casp3$^+$ (J) and TUNEL$^+$ (K) cells in the DAPI$^+$ cells in the LLC tumors in the absence or presence of SAA ($n = 5$). (L) Representative Doppler ultrasound images of LLC and B16F10 tumors following the treatment of Ctrl or SAA. (M, N) Quantitation for the percentages of average oxygen area of total area in the LLC (M) and B16F10 (N) tumors

treated group were significantly decreased compared with those in the vehicle control treated group (Supporting Information Fig. S1A and S1B). To further dissect the driving forces of restricted tumor growth under the pharmacological intervention of SAA, we thus performed the H&E staining and immunofluorescence analysis to determine the proliferation, apoptosis and necrosis fates of tumors. Notably, the proliferative rates of tumors as detected by the Ki67 staining were prominently diminished in the presence of SAA, whereas it was shown that SAA exerted no obvious impacts on the necrotic areas, nuclear atypia and cellular apoptosis in the tumors compared with vehicle control (Fig. 1G–K and Fig. S1C–S1G). In concomitant with these results, the percentage of G0/G1 subpopulations of tumor cells isolated from LLC tumors was significantly elevated, while the percentage of LLC cell populations located at in the S and G2/M phases was dramatically decreased following the treatment of SAA (Fig. S1H and S1I). Furthermore, no noticeable changes in body weight of mice and histopathology of organs including heart, liver, lung, and kidney were visualized between vehicle control and SAA-treated groups (Fig. S1J–S1M).

It has been highly appreciated that hypoxia and acidosis, serving as typical hallmarks of TME, are validated to be closely associated with unfavorable prognosis in cancer patients and play critical roles in driving tumor progression[30]. To this end, the hypoxia and acidosis of TME in the absence or presence of SAA were assessed accordingly. Strikingly, the Doppler ultrasound analysis revealed that SAA treatment contributed to significant enhancements in light of vascular perfusion and oxygenation in both LLC and B16F10 tumors compared with vehicle control treatment (Fig. 1L–N). Of note, the increases in these dynamic flow and perfusion by SAA treatment were observed throughout the whole tumors even in the cores of tumors (Fig. 1L). In line with the findings, pimonidazole (PIMO) as an effective reagent for detecting hypoxic regions *in vivo* was intravenously administrated into the LLC tumor-bearing mice, and the results of immunofluorescence staining highlighted that SAA potently attenuated the hypoxic area adjacent to tumor blood vessels (Fig. 1O and P). We subsequently detected the expression levels of HIF-1α and CA-9 as two classic hypoxia indicators in the tumors, and demonstrated that the expression levels of both HIF-1α and CA-9 were markedly mitigated after the treatment of SAA, indicating that SAA exerted a striking effect on reducing tumor hypoxia (Fig. 1O, Q, R, Fig. S1N and S1O). Additionally, there existed a conspicuous decrease in lactate levels of tumors in the SAA treated group compared with that in the vehicle control treated group (Fig. S1P). Taken together, our data implied that SAA played a pivotal role in suppressing tumor progression through ameliorating the hypoxia microenvironment in tumors.

3.2. SAA elicits tumor vascular normalization through improving vascular structure and function

It has been well accepted that tumor blood vessels are characterized by aberrant structure and lack coverage of mural cells that predominantly refer to pericytes and smooth muscle cells, which is inclined to impair vascular perfusion and aggravate vascular permeability and hypoxia[31]. In this regard, we sought to dissect whether the ameliorated hypoxia by SAA was associated with the alterations in tumor vascular structure and function. Therefore, we firstly analyzed the blood vessels in LLC tumors in detail following the treatment of SAA, and it was observed that, the number of blood vessels (CD31$^+$ staining) in the SAA-treated group was significantly less than that in the vehicle control group, suggesting SAA was capable of inhibiting tumor angiogenesis (Fig. 2A and B). To further understand the associations between ECs and mural cells in tumors upon SAA treatment, α-SMA and NG-2 were utilized to label the smooth muscle cells and pericytes, respectively. It was illustrated that the coverage of both smooth muscle cells and pericytes along the blood vessels in the LLC tumors was robustly elevated following the treatment of SAA, as validated by the co-staining of CD31/α-SMA and CD31/NG-2 (Fig. 2A and B). Moreover, the coverage of Col IV as an integral component of EC basement membrane was prominently augmented in the presence of SAA, indicative of enhanced basement membrane support. More interestingly, the deposition of fibrinogen around tumor blood vessels was fundamentally decreased when exposed to SAA, implying that SAA impeded the leaked fibrinogen from tumor blood vessels (Fig. 2C and D). Interestingly, in comparison to vehicle control, SAA was found to boost the expression level of an array of endothelial junctional molecules including VE-cad, ZO-1, β-Catenin, and Claudin-5 on tumor vessels, thereby enhancing the junction integrity in tumor blood vessels (Fig. 2C–F). Similarly, the decreased vascular density, elevated coverage of pericytes, enhanced basement membrane support, as well as tighten endothelial junctions that were reflected by increased expression levels of β-Catenin and Claudin-5 in tumor vessels were also observed in the B16F10 tumors in response to SAA treatment (Supporting Information Fig. S2A and S2B).

Next, we interrogated whether the structural alterations of tumor blood vessels challenged by SAA treatment were able to improve tumor vascular function. As anticipated, it was shown that there were limited blood vessels with FITC-lectin$^+$ staining in the vehicle control treated group, whereas the FITC-lectin$^+$ area in the blood vessels of LLC tumors in the SAA treated group was fundamentally escalated, suggesting that SAA exerted powerful function in potentiating vascular perfusion in the LLC tumor-bearing mice (Fig. 2G and H). More intriguingly, it was uncovered that the treatment of SAA overtly hampered the leakage of dextran from the surrounding blood vessels when compared with vehicle control, representing the decreased vascular permeability by SAA (Fig. 2G and H). Aiming at visualizing the leaked dye in a 3D manner, the tumors were harvested from the LLC tumor-bearing mice intravenously received TRITC-dextran and then the vascular leakage was examined with the two-photon microscopy. We found that SAA intervention was able to mitigate the area of leaked and diffused TRITC-dextran outside of the blood vessels and resulted in a significant increase in diameter of tumor blood vessels (Fig. 2I–K, Supporting Information Movies 1 and 2). Furthermore, scanning electron microscope (SEM) images pinpointed that SAA was capable of fortifying the vascular integrity with

---

($n = 3$). (O) Representative images of immunofluorescence co-staining for CD31 (red), PIMO (green) and DAPI (blue) (scale bars: 100 μm) as well as representative images of IHC staining for HIF-1α and CA-9 (scale bars: 200 μm) in the absence or presence of SAA. (P–R) Quantification for the percentages of PIMO$^+$ areas (P), HIF-1α^+ (Q), and CA-9$^+$ (R) area in the LLC tumors ($n = 5$). All data are presented as mean ± SD. Statistical analysis was performed using two-sided unpaired t-tests. *$P < 0.05$, **$P < 0.01$, ***$P < 0.001$, n.s: no significance *versus* Ctrl group.
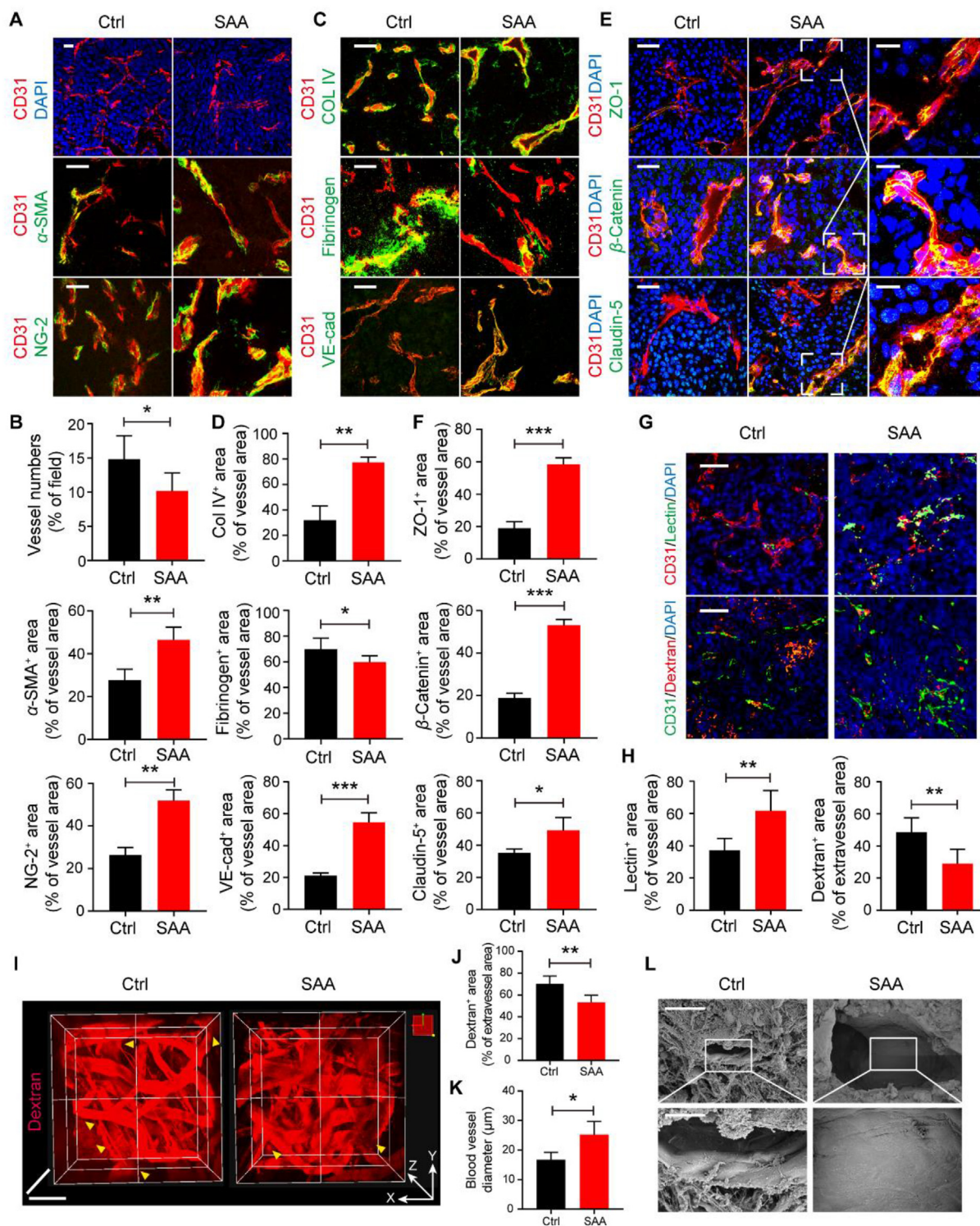
Figure 2 SAA elicits tumor vascular normalization. (A) Representative immunofluorescence images for co-staining of CD31 (red) with DAPI (blue), α-SMA (green) or NG-2 (green) in the LLC tumors treated with Ctrl and SAA. Scale bars: 100 μm. (B) Quantification for the number of blood vessels, as well as the percentage of CD31$^+$ α-SMA$^+$ area and CD31$^+$ NG-2$^+$ area in the LLC tumors (n = 5 or 6). (C) Representative immunofluorescence images for co-staining of CD31 (red) with Col IV (green), Fibrinogen (green) and VE-cad (green) in the LLC tumors treated with Ctrl and SAA. Scale bars: 100 μm. (D) Quantification for the percentage of CD31$^+$ Col IV + area, CD31$^+$ Fibrinogen + area, and CD31$^+$ VE-cad$^+$ area in the LLC tumors (n = 5). (E) Representative immunofluorescence images for co-staining of CD31 (red) with ZO-1 (green), β-Catenin (green) and Claudin-5 (green) in the LLC tumors treated with Ctrl and SAA. Scale bars: 100 μm; scale bars for zoom in: 20 μm. (F) Quantification for the percentage of CD31$^+$ ZO-1$^+$ area, CD31$^+$ β-Catenin$^+$ area, and CD31$^+$ Claudin-5$^+$ area in the LLC tumors (n = 5). (G) Representative immunofluorescence images of lectin perfusion (green) and leaked dextran (red) in the tumor blood vessels (stained with

tighten EC junctions, as shown by the flatten and continuous endothelium (Fig. 2L and Fig. S2C). Meanwhile, in order to investigate the impacts of SAA on normal vascular structure, the C57BL/6J mice were intraperitoneally injected with saline or SAA for consecutive 14 days, followed by the examination of pericyte coverage and endothelial tight junctions of normal blood vessels in the lung and liver tissues. We found that there was no obvious difference in pericyte coverage between control and SAA treated mice in both normal liver and lung tissues (Fig. S2D and S2E). Moreover, it was observed that SAA failed to influence the endothelial tight junctions compared to vehicle control in the normal lung tissues, which was reflected by both CD31/β-Catenin co-staining and CD31/Claudin-5 co-staining (Fig. S2F and S2G). Collectively, these findings manifested that SAA played a crucial role in inducing vascular normalization *via* correcting aberrant vascular structure and function.

Supplementary video related to this article can be found at https://doi.org/10.1016/j.apsb.2024.02.003

3.3. SAA accelerates the recovery of disrupted endothelial junctions induced by hypoxia

A growing body of evidence suggests that hypoxia-induced HUVECs serve as a reliable and robust approach to simulate the phenotypes of tumor vascular ECs since hypoxia is one of the fundamentally important features of solid tumors[32,33]. Surprisingly, it was revealed that SAA ranging from 20 to 80 μmol/L exhibited no conspicuous effect on the cell viability of HUVECs under the normoxic conditions, whereas the proliferative capability of HUVECs under hypoxia was considerably suppressed by SAA at a concentration of 80 μmol/L (Supporting Information Fig. S3A). In agreement with the results, the immunofluorescence staining for Ki67 unveiled that the proliferation of HUVECs under the hypoxic conditions appeared to be more sensitive to SAA treatment compared with that under normoxia (Fig. S3B). Likewise, HUVECs displayed reinforced abilities of migration and tube formation under the hypoxic conditions in comparison to those under normoxia, and SAA was capable of repressing the migration and tube formation of hypoxia-induced HUVECs in a dose-dependent manner (Fig. S3C−S3H). In order to further gain insight into the molecular mechanisms underlying that SAA influenced the biological behaviors of HUVECs under the hypoxic conditions, we thus performed the RNA-seq for hypoxia-induced HUVECs in the absence or presence of SAA to identify the genes that were significantly altered in ECs following the treatment of SAA. Notably, there were total 72 genes that were significantly upregulated and 64 genes that were dramatically downregulated in response to SAA when compared with vehicle control (Fig. 3A and B). More importantly, Kyoto encyclopedia of genes and genomes (KEGG) pathway enrichment analysis unraveled that differentially expressed genes were predominantly involved in the cellular processes including focal adhesion, gap junction, TJ and AJ (Fig. 3C). Moreover, GSEA delineated that

SAA treatment resulted in a dynamic bias towards a series of specific pathways that were associated with positive regulation of tight junctions and oxidative phosphorylation as well as negative regulation of oxidative stress (Fig. 3D).

Subsequently, we were inclined to shed light on whether SAA would be able to regulate the expression level of a panel of AJ and TJ proteins. Of interest, it was elucidated that both the expression levels of VE-cad as a key component of AJ and ZO-1 as an important regulator of TJ in the HUVECs were rigorously heightened upon the treatment of SAA (Fig. 3E−G). More intriguingly, it was deciphered that, in comparison to vehicle control, SAA was able to provoke extensive expression of β-Catenin at sites of cell−cell contacts but restricted its nuclear accumulation accompanied with the impaired phosphorylation level (Fig. 3H−J). Given that Claudin-5 has been known to be precisely regulated by β-Catenin[32], we also found that SAA rigorously bolstered the expression of Claudin-5 in HUVECs (Fig. 3H and K). Furthermore, the leaked Dextran across HUVEC barrier mediated by hypoxia was tremendously mitigated by SAA and hypoxia-induced damage of HUVEC electrical resistance was profoundly intensified upon SAA treatment, all of which implicated the enhancement of tighten endothelial junctions (Supporting Information Fig. S4A and S4B). Overall, in parallel with the role of SAA in modulating tumor vasculature in the tumor-bearing mice, SAA was able to improve the TJ of ECs and rescued the disruption of endothelial barrier caused by hypoxia.

3.4. SAA counteracts hypoxia-triggered oxidative stress and metabolic reprogramming in ECs

It has been well established that hypoxia has preference to enhance the degree of oxidative stress in ECs and further contribute to endothelial dysfunction[34,35]. On the basis of the RNA-seq data, we sought to explore whether the treatment of SAA was able to ameliorate the oxidative stress triggered by hypoxia in ECs. In this sense, we measured the levels of multiple indicators of oxidative stress in the HUVECs and identified their difference between normoxic and hypoxic conditions in the absence or presence of SAA. Intriguingly, it was delineated that hypoxic conditions curtailed the concentrations of SOD, CAT, and GSH-Px that represent their activities compared with the normoxic conditions, all of which could be reversed following the treatment of SAA (Fig. 4A−C). In addition, in comparison to normoxia, hypoxia was also able to confer a remarkable increase in MDA content, which was rescued in the presence of SAA (Fig. 4D). Consistent with these observations, although reduced levels of ROS and total superoxide were encountered in hypoxia compared with normoxia, SAA treatment was capable of dose-dependently attenuating their levels under the hypoxic conditions (Fig. 4E and Fig. S4C). Due to the fact that Keap1/Nrf2 signaling cascade is known to be deeply involved in the adaption and survival of cells under the circumstance stress[36], we therefore assessed whether the transduction of this signaling was related to the altered oxidative stress in hypoxia by SAA. Indeed,

---

CD31). Scale bars: 100 μm. (H) Quantification for the percentage of lectin$^+$ area in the vessel area and the percentage of dextran$^+$ area in the extravascular area ($n = 5$). (I) Two-photon intravital microscopy images of the LLC tumors intravenously received dextran in the Ctrl and SAA treated groups. Scale bars for x axis: 50 μm and scale bars for z axis: 200 μm. (J, K) Quantification for dextran$^+$ area of extravascular area (J) and diameter of tumor blood vessels (K) in the LLC tumor-bearing mice treated with Ctrl and SAA ($n = 4$). (L) Representative SEM images for the tumor blood vessels in the LLC tumors. Scale bars: 30 μm (upper panel) and 10 μm (lower panel). All data are presented as mean ± SD. Statistical analysis was performed using two-sided unpaired t-tests. *$P < 0.05$, **$P < 0.01$, ***$P < 0.001$ *versus* Ctrl group.
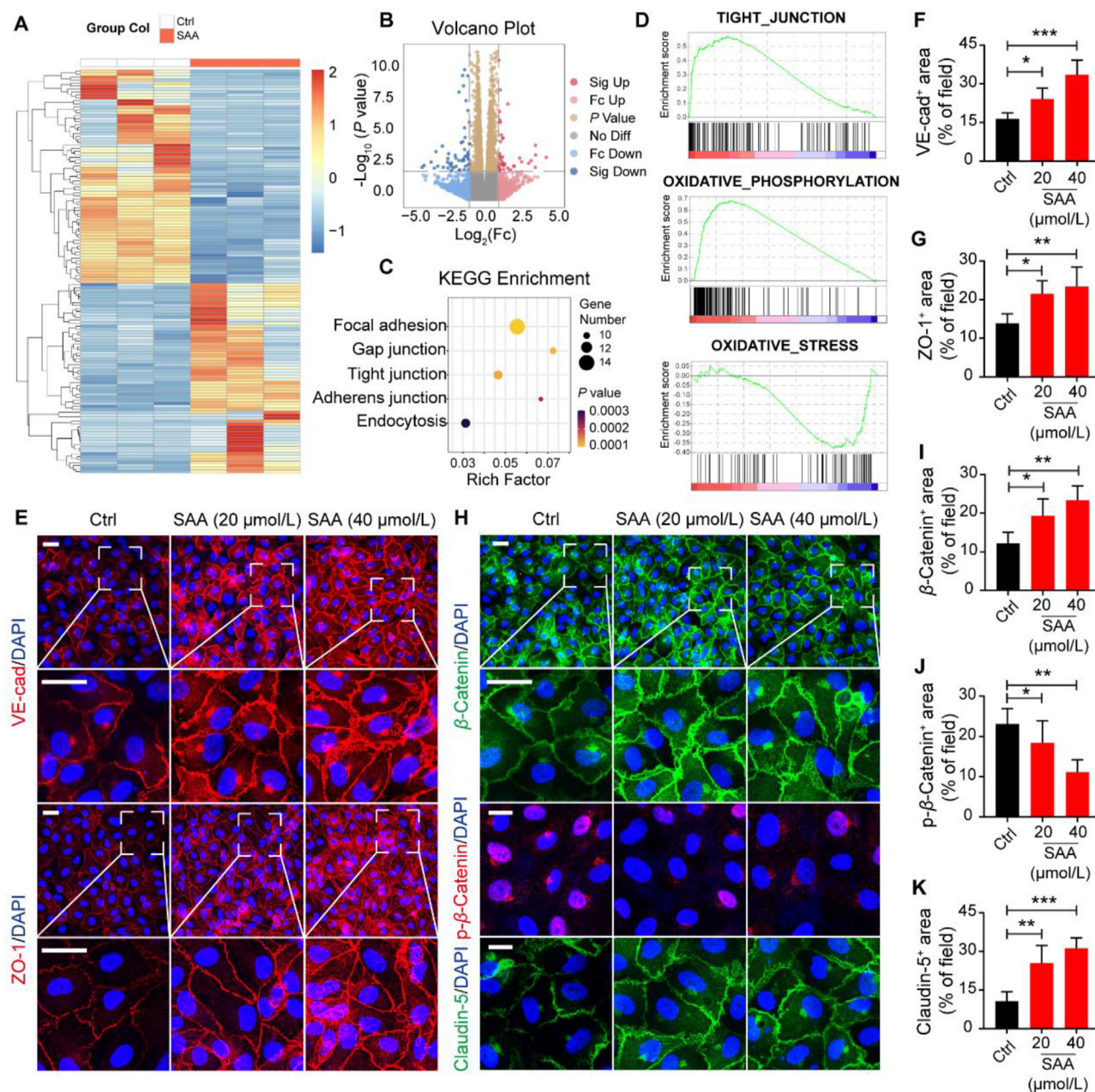
Figure 3 SAA accelerates the recovery of disrupted endothelial junctions induced by hypoxia. (A) Heatmap showing the genes that were significantly differently expressed between Ctrl and SAA treated HUVECs induced by hypoxia. (B) Volcano plot displaying the differentially expressed genes. (C) KEGG enrichment analysis showing the core signaling pathways based on the differently expressed genes. (D) GSEA was performed to analyze clusters of genes that belong to tight junction, oxidative stress, and oxidative phosphorylation. (E) Representative immunofluorescence images for VE-cad (red)/DAPI (blue) and ZO-1 (red)/DAPI (blue) in the HUVECs. Scale bars: 20 μm; scale bars for zoom in: 20 μm. (F, G) Quantification for the percentage of VE-cad$^+$ area (F) and ZO-1$^+$ area (G) in the visual field ($n = 6$). (H) Representative immunofluorescence images for β-Catenin (green)/DAPI (blue), p-β-Catenin (red)/DAPI (blue), and Claudin-5 (green)/DAPI (blue) in the HUVECs. Scale bars: 20 μm; scale bars for zoom in: 20 μm. (I−K) Quantification for the percentage of β-Catenin$^+$ area (I), p-β-Catenin$^+$ area (J), and Claudin-5$^+$ area (K) in the visual field ($n = 6$). All data are presented as mean ± SD. Statistical analysis was performed using ordinary one-way ANOVA. *$P < 0.05$, **$P < 0.01$, ***$P < 0.001$ *versus* Ctrl group.

when compared with normoxia, hypoxia reinforced the protein expression of Keap1, but mitigated the protein levels of Nrf2 as well as its downstream proteins including HO-1 and NQO1 in the HUVECs (Fig. 4F and G). Nevertheless, the treatment of SAA could decline the protein expression of Keap1 while escalating the protein levels of Nrf2, HO-1 and NQO1 in the HUVECs under the hypoxic conditions (Fig. 4F and G). Likewise, the mRNA levels of

NRF2, *HO1* and *NQO1* in the HUVECs upon hypoxia were conspicuously elevated in response to SAA (Fig. S4D). Taken together, these data highlighted that SAA alleviated the oxidative stress level of ECs under hypoxic conditions.

It has been widely held that hypoxia-associated signaling cascades and metabolic alterations are tightly interconnected[37]. To further exploit the metabolic profiles of HUVECs following the
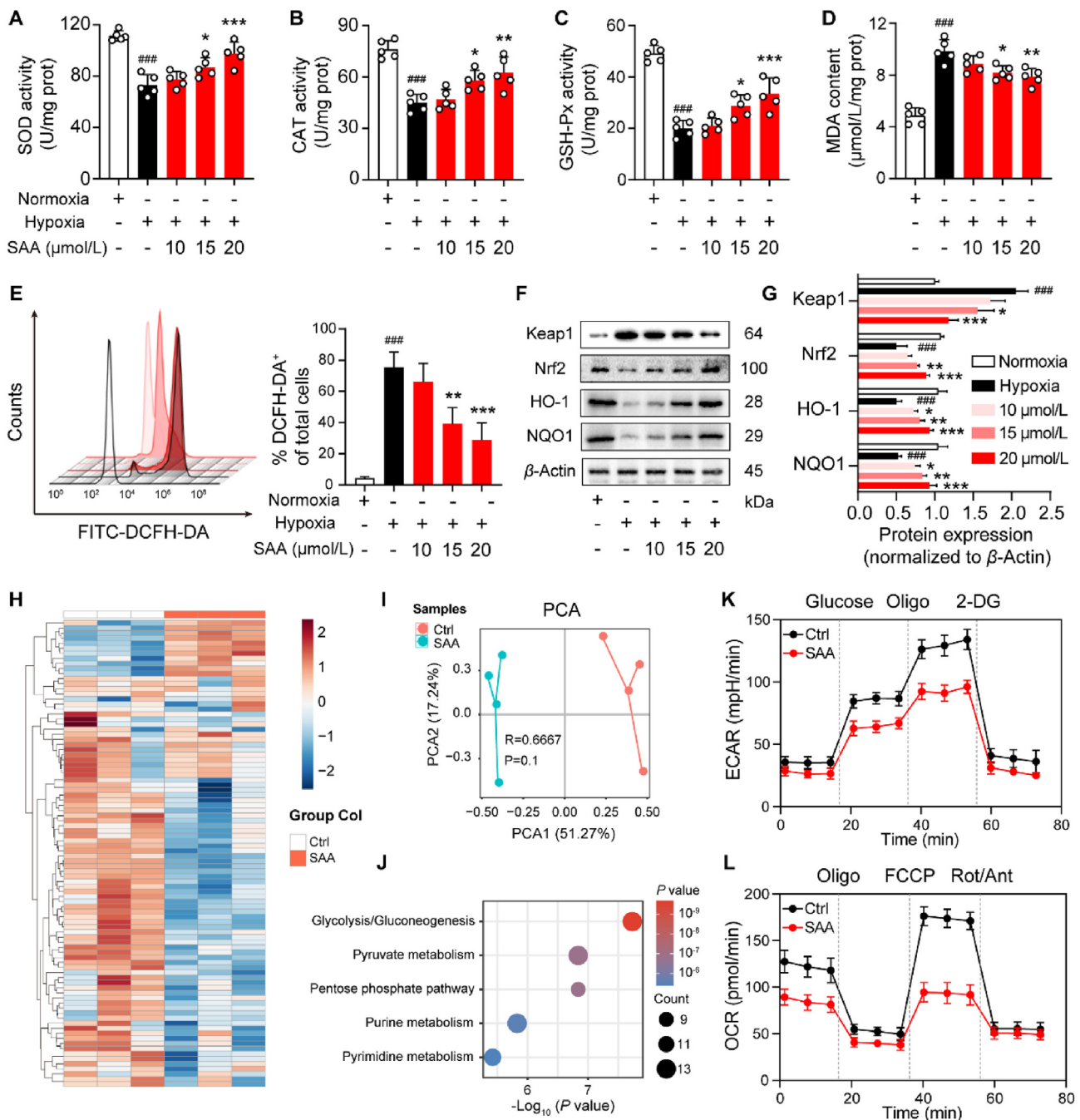
Figure 4   SAA counteracts hypoxia-triggered oxidative stress and metabolic reprogramming in ECs. (A–D) The contents of oxidative stress markers including SOD (A), CAT (B), GSH-Px (C), and MDA (D) in hypoxia-stimulated HUVECs treated various concentrations of SAA ($n = 5$). (E) The production of ROS was detected using the DCFH-DA fluorescent probe ($n = 3$). (F) The protein expression levels of Keap1, Nrf2, HO-1, and NQO1 were determined by Western blot analysis. (G) Quantification of densitometric ratios for the protein expression levels of Keap1, Nrf2, HO-1, and NQO1 ($n = 3$). β-Actin was used as a loading control. (H) Heatmap showing the metabolites that were significantly different between Ctrl and SAA treated HUVECs stimulated by hypoxia. (I) PCA of metabolites in the HUVECs stimulated by hypoxia in the Ctrl and SAA treated groups. (J) Enrichment analysis of metabolites. (K, L) Representative traces of ECAR (K) and OCR (L) values were quantified by the seahorse assay ($n = 3$). All data are presented as mean ± SD. Statistical analysis was performed using ordinary one-way ANOVA. [###]$P < 0.001$ *versus* normoxia group. *$P < 0.05$, **$P < 0.01$, ***$P < 0.001$ *versus* hypoxia Ctrl group.

treatment of SAA, non-targeted metabolomics analysis was thus employed to discern the impacts of SAA on hypoxia-mediated metabolic reprogramming in the HUVECs. The detailed data of non-targeted metabolomics heatmap displayed notable metabolic differences in the HUVECs under the hypoxic conditions between

vehicle control and SAA-treated groups (Fig. 4H). More specifically, the results unveiled that SAA treatment significantly diminished the contents of glycolytic metabolites (Fig. S4E), but profoundly replenished the levels of oxidative phosphorylation-associated metabolites in the HUVECs stimulated by hypoxia

(Fig. S4F). Further, principal component analysis (PCA) pin-pointed that there was compelling separation along PCA1 in the HUVECs between vehicle control and SAA-treated groups (Fig. 4I). Metabolic pathway analysis revealed that glycolysis/gluconeogenesis, pyruvate metabolism, and pentose phosphate pathway were strikingly changed in response to SAA under hypoxia (Fig. 4J). Meanwhile, seahorse analysis showed that SAA was prone to largely inhibit the levels of glycolysis and mito-chondrial oxidative respiration (Fig. 4K and L, and Fig. S4G & S4H). Hence, these findings implicated that SAA antagonized endothelial glycolysis triggered by hypoxia and drove metabolic reprogramming.

3.5. SAA limits endothelial glycolysis via binding to PKM2

Next, we intended to dissect and identify the cellular targets of SAA that mediated its pharmacological functions in ECs. Owing to the relatively simple chemical structure of SAA (Supporting Information Fig. S5A), the DARTS assay, emerges as an effec-tive and efficient method to excavate the direct targets for ligands without additional modifications[38,39], was utilized to unlock the potential candidates that are able to interact with SAA. In this regard, we therefore incubated the HUVEC lysates with SAA, and observed a Coomassie blue-stained band at 60 kDa where SAA appeared to be more abundant than other sites (Fig. S5B). Note-worthily, the MS analysis deciphered that PKM2 exhibited the highest relative abundance compared with other proteins, and it was extensively enriched in the SAA-treated group rather than the vehicle control treated group (Fig. 5A and B), all of which sug-gested that PKM2 might act as the predominantly target protein of SAA. Conventionally, PKM is deemed to be a rate-limiting glycolytic enzyme that catalyzes the conversion of phosphoenol-pyruvate to pyruvate[40] (Fig. 5C), we thus examined the activities of a list of glycolytic enzymes including PK. It was found that SAA was capable of repressing the activity of PK in a dose-dependent manner, but failed to influence the activities of hexo-kinase and phosphofructokinase (Fig. 5D, and Fig. S5C & S5D). As expected, in comparison to vehicle control, the most obviously changed metabolic pathway by SAA was glycolysis, in particu-larly a significant decrease of pyruvate concentration following the treatment of SAA was observed (Fig. 5E). Of interest, the cellular thermal shift assay (CETSA) data elucidated that there were direct interactions between SAA and PKM2 (Fig. 5F), which was substantiated by the results of SPR analysis that showed the direct binding of SAA and PKM2 with a K_d value of 1.54 μmol/L (Fig. 5G). Furthermore, the expression level of PKM2 tetramer was mitigated while the relative level of PKM2 dimer was upre-gulated following the treatment of SAA (Fig. 5H). Despite that the expression of cytosolic PKM2 in the HUVECs remained un-changed in the presence of SAA (Fig. 5I), its nuclear translocation was prominently accumulated by SAA treatment (Fig. 5J and K). As such, our data illustrated that SAA directly interacted with PKM2 in the HUVECs.

Aiming at inspecting the possible binding sites of SAA on PKM2, subsequent molecular docking analysis was performed to unveil the binding mode with an established structure of PKM2 (PDB: 1T5A, Fig. 6A and B). Interestingly, it was predicted that the structure of SAA could successfully fit in the catalytic domain and generate interactions with multiple residues in the interior of PKM2, which turned out to be Arg489, Gly520 and Lys433. To this end, different mutant plasmids of PKM2 were constructed to verify the precise binding sites with SAA that mediated the

downstream effects (Fig. S5E). Surprisingly, it was elaborated that transfection with K433A mutated plasmid was able to reverse the inhibited PK activity and pyruvate content by SAA. However, the R489A and G520A mutated plasmids failed to rescue the effects of SAA (Fig. 6C and D). Further, the dimerization of PKM2 induced by SAA was antagonized upon K433A mutation (Fig. 6E). Also, K433A mutation reversed the boosted nuclear accumulation of PKM2 stimulated by SAA (Fig. 6F and G). Additionally, the MS analysis emphasized that K433-containing peptide harbored a corresponding mass shift in the peptide spectra of the SAA-treated group (Supporting Information Fig. S5F and Table S4). More importantly, SAA was able to bind to PKM2 wild type protein in a dose-dependent manner (Fig. 6H). Conversely, the PKM2 protein with K433A mutation displayed almost no binding affinity, even with the increased concentrations of SAA (Fig. 6H). All of these data suggested that SAA relied on Lys433 residue to regulate PKM2 activity. To further define the structural stability of the SAA−PKM2 binding complex, the 100 ns molecular dynamics simulation was carried out to discern whether SAA could exert an allosteric regulation on PKM2. It was shown that SAA was capable of tightening the PKM2 domain and adjusting its conformation (Fig. 6I). Moreover, the time evolution of weighted root mean square deviation (RMSD) stated that, in comparison to PKM2 alone, RMSD of PKM2 appeared to be more unstable and elevated upon bound to SAA (Fig. 6J). The root mean square fluctuation (RMSF) of PKM2 also demonstrated more flexibility when bound to SAA, implying the overall fluc-tuation and residual flexibility trend of PKM2 (Fig. 6K). Conse-quently, Lys433 residue of PKM2 was required for its interactions with SAA and SAA tended to alter the conformation of PKM2 to form a complex system.

3.6. SAA strengthens β-Catenin/Claudin-5 axis-mediated endothelial TJ

In order to investigate the clinical relevance between the expres-sion of tumor endothelial PKM2 and tumor progression, we characterized the expression pattern of PKM2 in 14 human lung carcinoma specimens with low or high differentiation (Supporting Information Fig. S6A and S6B). Of note, the elevated expression of PKM2 was visualized in the tumor area of lung tissue compared with that in the normal lung tissues, and PKM2 expression was extensively co-localized with the expression of CD31 (Fig. 7A and C). It was observed that tumor endothelial PKM2 was strongly expressed in the poorly differentiated lung tumor tissues compared with that in the well differentiated lung tumor tissues (Fig. 7A and C). More intriguingly, the expression levels of β-Catenin and Claudin-5 in the tumor blood vessels were fundamentally impaired in the poorly differentiated lung tumors, indicating extremely aberrant tumor vasculature with loosen endothelial junctions (Fig. 7B and C). Further, we examined the mRNA expression levels of a collection of EC junctions-associated genes including *PECAM1*, *CDH5*, *CLDN1*, *CLDN5*, *TJP1*, and *TPJ2* in the lung tumor tissues, and it was revealed that there were sig-nificant differences in light of the mRNA expression levels of *PECAM1*, *CDH5*, *CLDN5*, and *TJP1* between poorly and well differentiated lung tumor tissues (Fig. 7D).

It has been documented that PKM2 in low enzymatic activity is inclined to act as a coactivator of β-Catenin, which engages with TCF4 to participate in transcriptional regulation of a plethora of genes including *CLDN1* and *CLDN5* that have impacts on EC junction fate[41−43]. As such, we sought to determine whether SAA
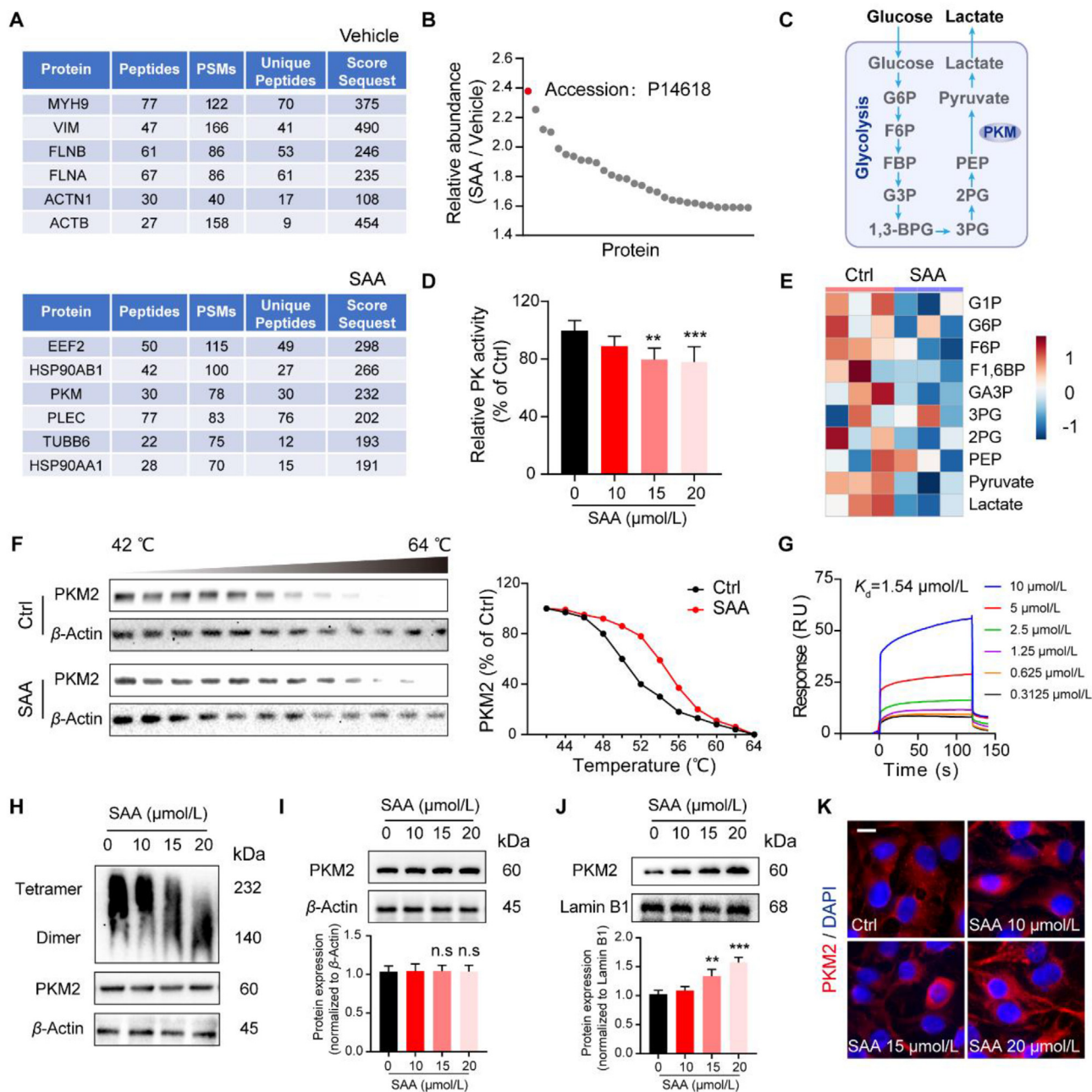
Figure 5 SAA limits endothelial glycolysis *via* binding to PKM2. (A) MS-based DARTS sequencing of associated proteins was performed to identify the targets of SAA (top: Vehicle, bottom: SAA). (B) Relative abundance of SAA target protein candidates. (C) Schematic diagram of glycolysis. (D) Relative PK activity was measured by the kinase reagent kit ($n = 5$). (E) Heatmap showing the glycolytic metabolites that were significantly different between Ctrl and SAA-treated HUVECs upon hypoxia ($n = 3$). (F) HUVECs were incubated with or without SAA for 2 h, the cells were then subjected to temperature-dependent CETSA for PKM2. (G) Binding affinities of SAA to PKM2 were measured by SPR. (H) The cell lysates were treated with SAA, and then subjected to non-reducing gradient gel electrophoresis to detect the dimerization of PKM2. (I) Western blot analysis showing the protein expression of cytosol PKM2. The densitometric ratios of bands for cytosol PKM2 were quantified. β-Actin was used as a loading control. (J) Western blot analysis showing the protein expression of nuclear PKM2. The densitometric ratios of bands for nuclear PKM2 were quantified. Lamin B1 was used as a loading control. (K) Immunofluorescence images for endogenous PKM2 (red)/ DAPI (blue) in the HUVECs treated with various concentrations of SAA. Scale bars: 10 μm. All data are presented as mean ± SD. Statistical analysis was performed using ordinary one-way ANOVA. **$P < 0.01$, ***$P < 0.001$, n.s: no significance *versus* Ctrl group.

was able to modulate the transactivation function of β-Catenin through propelling PKM2 entry into the nucleus. Noteworthily, SAA was capable of orchestrating the nuclear translocation of PKM2 and β-Catenin, as well as lowering the phosphorylation

level of β-Catenin (Figs. 3H and 5J). Likewise, SAA upregulated the mRNA expression levels of *CTNNB* and its downstream target genes including *TCF4*, *CLDN1*, and *CLDN5* (Fig. 7E). Additionally, Co-immunoprecipitation (Co-IP) analysis supported that
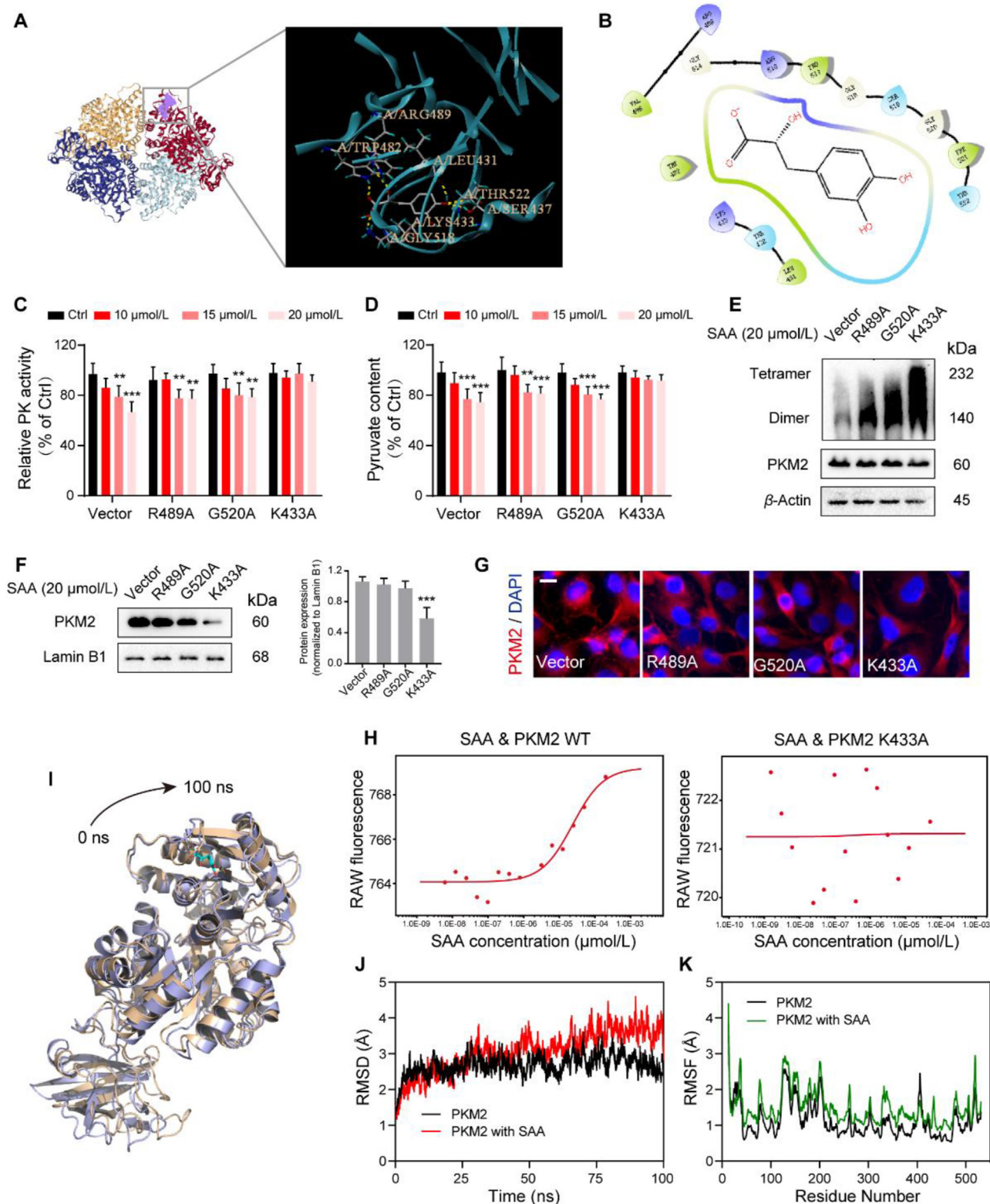
Figure 6 Lys433 of PKM2 is required for its binding to SAA. (A) The interactions between SAA and PKM2 were predicted using molecular docking analysis. (B) The potential binding sites of SAA to PKM2 were predicted. (C, D) HUVECs were transfected with empty vector, as well as Arg489, Gly520 and Lys433 mutation plasmids and then cultured with various concentrations of SAA under hypoxia. Relative PK activity (C) and pyruvate content (D) were detected using relevant kits ($n = 5$). (E) The cell lysates were treated with SAA at the dosage of 20 μmol/L, and subjected to non-reducing gradient gel electrophoresis to examine the dimerization of PKM2 with mutations of different residues. (F) Western blot analysis showing the protein expression of nuclear PKM2. The densitometric ratios of bands for nuclear PKM2 were quantified. Lamin B1 was used as a loading control. (G) Immunofluorescence image for endogenous PKM2 (red)/DAPI (blue). Scale bars: 10 μm. (H) MST assay showing

SAA treatment potentiated the binding of β-Catenin to PKM2 (Fig. 7F), and the interactions between β-Catenin and TCF4 were also intensified following the treatment of SAacA (Fig. 7G). To further decipher whether PKM2 was involved in the SAA-mediated influence on β-Catenin/Claudin-5 axis, we initially transfected the PKM2 siRNA into the HUVECs and validated the knockdown efficiency (Fig. S6C−S6E). RNA-seq was subsequently performed in the HUVECs upon hypoxia following the silence of PKM2 expression. Interestingly, SAA failed to yield a collective up-regulation in the mRNA levels of AJ and TJ associated molecules in the HUVECs with PKM2 knockdown (Fig. S6F). Meanwhile, although silence of PKM2 mitigated the activity of PK and content of pyruvate compared with scramble control, no additive effects were found when SAA treatment in combination with PKM2 knockdown (Fig. S6G and S6H). Furthermore, regardless of SAA treatment, knockdown of PKM2 in the HUVECs under the hypoxic conditions could not significantly change the expression levels of β-Catenin and p-β-Catenin in the nucleus (Fig. 7H−K). Meanwhile, SAA intervention failed to boost the expression of Claudin-5 in the PKM2-silenced HUVECs (Fig. 7L and M). Similarly, SAA was not able to regulate the mRNA expression levels of *CTNNB* and its downstream target genes in the absence of PKM2 (Fig. 7N). Furthermore, although SAA alone could rescue the loss of endothelial barrier integrity provoked by hypoxia, the damaged endothelial barrier was not changed following the silence of PKM2 in the absence or presence of SAA, which indicated that the restored endothelial integrity by SAA relied on the presence of PKM2 (Fig. S6I and S6J). Ultimately, SAA improved endothelial TJ through regulating β-Catenin/Claudin-5 signaling axis in a PKM2-dependent manner.

3.7. SAA propels the delivery of DOX into tumors and magnifies the anti-tumor effect

It has been well established that tumor vascular normalization with enhanced vascular structure and function plays a pivotal role in enhancing chemotherapy delivery and efficacy against tumor progression[7,44,45]. In this sense, we further explored whether a combination treatment of SAA and chemotherapeutic agent DOX, which belongs to an anthracycline family member that induces cell cycle arrest[46], could boost the efficacy against tumor progression. As such, SAA treatment was initiated when the tumors became palpable and continued for 7 days for triggering vascular normalization, followed by the treatment of DOX. Of interest, our results uncovered that SAA in combination with DOX was capable of significantly repressing the volumes and weights of subcutaneous LLC and B16F10 tumors as compared to vehicle control or DOX alone (Fig. 8A−C and Supporting Information Fig. S7A−S7E). Additionally, in comparison to DOX monotherapy, the combination therapy of SAA and DOX gave rise to more conspicuous anti-tumor effect accompanied by limited proliferation as well as elevated necrosis and apoptosis of tumors (Fig. 8D−H and Fig. S7F−S7K). To further ascertain whether the synergistic inhibitory effects of SAA and DOX on tumor progression *in vivo* was correlated to direct inhibition on tumor cells,

we thus treated the LLC tumor cells with vehicle control, SAA, DOX or SAA plus DOX, and then found that combination treatment of SAA and DOX exerted no obvious inhibitory effect on the proliferation of LLC cells *in vitro* compared with SAA or DOX alone (Fig. S7L).

Considering that it was showed that SAA treatment alone failed to augment apoptosis, we postulated that the slight increase in the expression levels of Cl-Casp3 and transferase dUTP nick end labeling (TUNEL) in the combination treatment group might be owing to the presence of DOX. In this perspective, we further intended to explore whether the increases in perfusion and dilation of blood vessels were sufficient to improve the delivery of DOX into tumors. Two-photon microscopy imaging unraveled that the vascular perfusion, blood vessel diameter, and delivery of DOX in the LLC tumors were all augmented in the combination treatment group as compared to those in the DOX alone treated group (Fig. 8I−K and Supporting Information Movies 3 and 4), implicating that SAA treatment incited tumor vascular remodeling to pave the way for the delivery of DOX into tumors. Further immunofluorescence staining confirmed that the intratumoral DOX level was robustly boosted in the mice treated with SAA and DOX when compared to the mice treated with DOX alone (Fig. 8L and M, and Supporting Information Fig. S8A & S8B). Meanwhile, the concentrations of DOX within tumors were detected by liquid chromatography (LC)/MS. The tumor tissues of LLC tumor-bearing mice were collected at 60 min and 90 min following the last administration of DOX, and it was observed that the concentrations of DOX at different time points upon the combination treatment of SAA and DOX were significantly higher than that upon the treatment of DOX alone (Fig. S8C−S8F). Furthermore, it was observed that SAA increased the expression of PKM2 in the nucleus of tumor ECs (Fig. S8G−S8I), providing the *in vivo* evidence to support that PKM2 was required for SAA-mediated tumor vascular normalization. Of note, the side effects caused by continuous infusion of DOX, such as cardiotoxicity, cannot be ignored[47]. Compared with vehicle control, DOX resulted in significant loss of body at the late stage of experimental period, whereas SAA was able to delay the DOX-induced body weight loss (Fig. S8J). Moreover, the heart weight and various pathological alterations provoked by DOX were potently relieved in the presence of SAA (Fig. S8K and S8L). Altogether, our data proposed that SAA treatment was capable of eliciting tumor vascular normalization, thereby contributing to enhanced chemotherapeutic drug delivery and efficacy against tumor progression.

Supporting video related to this article can be found at https://doi.org/10.1016/j.apsb.2024.02.003

4. Discussion

It has been well recognized that tumor vasculature has profound consequences on influencing tumor progression. Tumor blood vessels with aberrant structure and function pose considerable challenges for the delivery and efficacy of chemotherapy and immunotherapy. Hence, seeking promising agents to fulfill tumor vascular normalization has been gaining increasing attention. SAA

---

the binding affinities of SAA to PKM2 WT and PKM2 K433A proteins. (I) The presentative conformation of PKM2 protein binding with SAA upon molecular dynamics simulation. (J) The time evolution of RMSD values for PKM2 protein in the absence or presence of SAA. (K) Calculation of RMSF for PKM2 protein in the absence or presence of SAA. All data are presented as mean ± SD. Statistical analysis was performed using ordinary one-way ANOVA. **$P < 0.01$, ***$P < 0.001$, n.s: no significance *versus* Ctrl and Vector group.
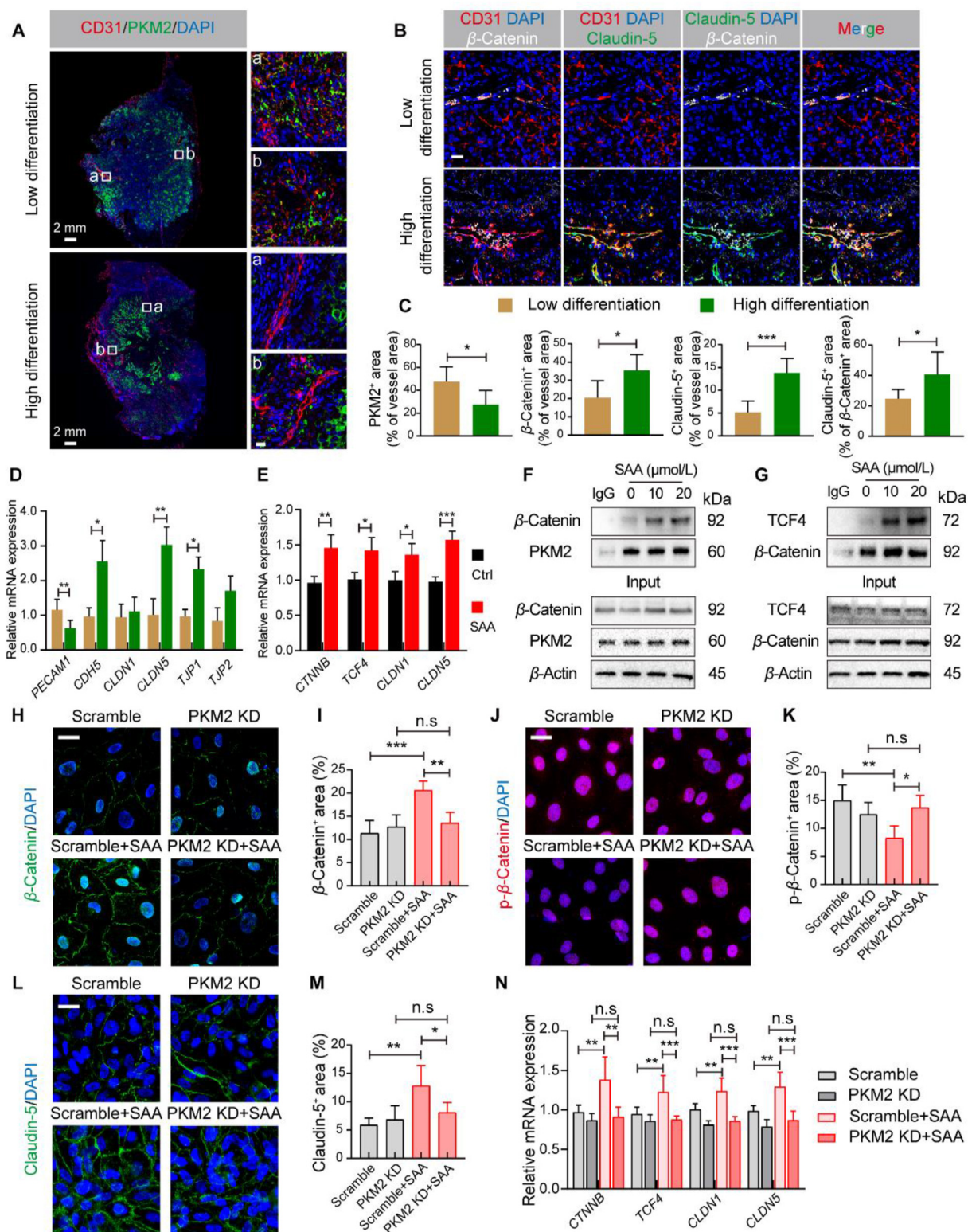
Figure 7 SAA strengthens β-Catenin/Claudin-5 axis-mediated endothelial TJ. (A) Representative immunofluorescence images for CD31 (red), PKM2 (green), and DAPI (blue) in the human lung cancer samples. Scale bars (left): 2 mm; scale bars for the zoom area (right): 20 μm. (B) Representative immunofluorescence images for CD31 (red), Claudin-5 (green), β-Catenin (white) and DAPI (blue) in the human lung cancer samples. Scale bar: 20 μm. (C) Quantification for the percentage of CD31$^+$ with PKM2$^+$, β-Catenin$^+$, or Claudin-5$^+$ area as well as the percentage of β-Catenin$^+$ Claudin-5$^+$ area (n = 4 or 5). (D) Quantification for the mRNA expression levels of *PECAM1*, *CDH5*, *CLDN1*, *CLDN5*, *TJP1*, and *TJP2* in the human lung cancer tissues (n = 4−6). (E) Quantification for the mRNA expression levels of *CTNNB*, *TCF4*, *CLDN1*, and *CLDN5* in the HUVECs treated with or without SAA (n = 4−6). (F) Representative Co-IP analysis for β-Catenin and PKM2 in the HUVECs.

as a major water-soluble phenolic ingredient isolated from *S. miltiorrhiza* has been found to harbor multiple pharmacological activities[48]. In the present study, we demonstrate that SAA is able to correct the abnormalities of tumor blood vessels as reflected by the improved vascular organization and function through blocking the EC glycolysis that may act as the engine of tumor angiogenesis. To some extent, the enhancement of tumor vascular structure and function by SAA alleviates the hypoxia in tumors, which further lowers the oxidative stress of ECs. The fulfilled tumor vascular normalization in response to SAA also provides favorable conditions for the delivery and efficacy of chemotherapy. Mechanistically, SAA is capable of binding to PKM2 and promoting the dimerization and nuclear translocation of PKM2 to strengthen the TJ of ECs *via* modulating the β-Catenin/Claudin-5 signaling axis.

Indeed, ECs in tumors tend to stimulate glycolysis in the process of angiogenesis that meets their requirements of rapid proliferation and increased migration, thereby resulting in structural abnormality and dysfunction of tumor blood vessels[13]. ECs are deemed to fundamentally differ from tumor cells, in which metabolism is frequently reprogrammed by hyperactivated signaling pathways rooted in oncogenomic alterations with the propose of proliferating in an uncontrolled manner[49]. Nonetheless, proliferating ECs are able to switch back to quiescent status, without provoking cellular demise when key growth factor signaling cascades are impaired[13]. More interestingly, tumor ECs appear to be more glycolytic and exhibited higher level of 6-phosphofructo-2-kinase/fructose-2,6-biphosphatase 3 (PFKFB3) compared with normal ECs. Deletion of a single PFKFB3 allele in ECs or utilization of a low dosage of a PFKFB3 inhibitor is sufficient to normalize the abnormal tumor blood vessels, prevent metastasis as well as synergize with chemotherapy without influencing tumor cells even though either of the strategy can only mitigate endothelial glycolysis by only 15%−20%[12]. In this study, we surprisingly elucidated that SAA is capable of targeting PKM2, a critical kinase of endothelial glycolysis, thereby triggering tumor vascular normalization. Despite that the role of PKM2 as a spy in tumors seems to be controversial[21], PKM2 mediated endothelial metabolism is worthy of detailed research. Consistent with the previous studies, it has been recently uncovered that inhibition of PKM2 is inclined to accelerate the substrate flux *via* the pentose phosphate pathway to produce the reducing equivalents and further protect against oxidative stress[22]. In addition, a growing body of evidence has unveiled the significance of glycolysis in the formation of blood vessels[50,51], thus further underscoring the therapeutic potential of targeting this metabolic pathway is gaining increasing attention.

It has been accepted that ECs act as highly plastic cells and have preference to rapidly respond to changing environmental circumstances[10]. This hypoxia-mediated metabolic reprogramming is essential for meeting the requirements of cellular energy under hypoxic stress[52]. At the transcriptional level, the metabolic switch tends to be governed by multiple signals including HIF-1α that gives rise to an elevated expression of glycolytic enzymes. CA-9 can also be profoundly influenced by HIF-1α with a metabolic shift to glycolysis[53]. Also, another hallmark of hypoxia has thought to be ROS formation, which results in the diminished expression of Nrf2 as a classic antioxidant modulator[54]. Nrf2 acts as an imperative transcription factor that is attributed to maintain oxidative homeostasis by virtue of binding to a negative regulator named Keap1[54]. It has also been documented that hypoxia contributes to a rapid and remarkable elevation in ROS level, along with the accumulation of HIF-1α as well as the activation of PKC and PI3K signaling, thereby exerting striking effect on augmenting glycolysis in the ECs under low oxygen tension conditions[55]. Our data pinpointed that the boosted protein expression of Nrf2 by SAA in the HUVECs under hypoxia was responsible for the degradation of Keap1, accompanied with the increased protein expression levels of HO-1 and NQO1. Through potentiating the degradation of Keap1, SAA was able to strengthen the protein stability of Nrf2, which could well define the role of SAA in Nrf2 induction in the ECs. Concurrently, SAA repressed the accumulation of ROS in the HUVECs under hypoxia, largely dependent on induction of Nrf2. As such, we speculate that the activation of Nrf2 signaling tends to be beneficial to the endothelial homeostasis and has robust impacts on anti-angiogenic therapy.

In fact, PK catalyzes the last and physiologically irreversible step of glycolysis and there are four types of PK isoforms in mammals including PKM1, PKM2, PKL and PKR[22,56]. Despite that PKM1, PKM2, PKL and PKR all possess a tetrameric form and present PK activity, only PKM2 harbors both a dimeric form and a tetrameric form[57]. When PKM2 is located at the tetrameric state, it exhibits a stronger affinity to its substrate PEP and further shows a higher PK activity, thereby catalyzing the generation of pyruvate by PEP[40]. PKM2 can also stay at a dimer state with low PK activity, and the dimeric PKM2 is able to enter into the nucleus to induce the transcription of various genes[40]. In light of glycolytic enzyme function of PKM2, PKM2 specially binds to the proteins that act as targets of proliferation-inducing tyrosine kinases and ultimately induces a reduction in the enzymatic activity of PKM2[40,57]. A growing body of evidence has uncovered that PKM2 also emerges as a direct substrate of these tyrosine kinases. For instance, fibroblast growth factor receptor 1 (FGFR1) phosphorylates PKM2 on Y105 to reduce the enzyme activity of PKM2[58]. Acetylation of PKM2 at K305 residue both mitigates PKM2 activity and targets it for lysosomal-dependent degradation[59]. Furthermore, oxidation of C358 residue of PKM2 reduces its activity and enables it to be sensitive to the oxidative stress[60]. In addition to its accepted role in metabolism, alternative non-metabolic functions of PKM2 have also been documented[61,62]. PKM2 has been reported to regulate the expression of numerous genes *via* serving as a protein transactivator along with HIF-1α or

(G) Representative Co-IP analysis for TCF4 and β-Catenin in the HUVECs. (H) Representative immunofluorescence images for β-Catenin (green)/DAPI (blue) in the HUVECs. Scale bars: 20 μm. (I) Quantification for the percentage of β-Catenin$^+$ area in the visual field ($n = 6$). (J) Representative immunofluorescence images for p-β-Catenin (red)/DAPI (blue) in the HUVECs. Scale bars: 20 μm. (K) Quantification for the percentage of p-β-Catenin$^+$ area in the visual field ($n = 6$). (L) Representative immunofluorescence images for Claudin-5 (green)/DAPI (blue) in the HUVECs. Scale bars: 20 μm. (M) Quantification for the percentage of Claudin-5$^+$ area in the visual field ($n = 6$). (N) Quantification for the mRNA expression levels of *CTNNB*, *TCF4*, *CLDN1*, and *CLDN5* in the HUVECs in different groups ($n = 4−6$). All data are presented as mean ± SD. Statistical analysis was performed using two-sided unpaired *t*-tests or ordinary one-way ANOVA. *$P < 0.05$, **$P < 0.01$, ***$P < 0.001$, n.s: no significance.
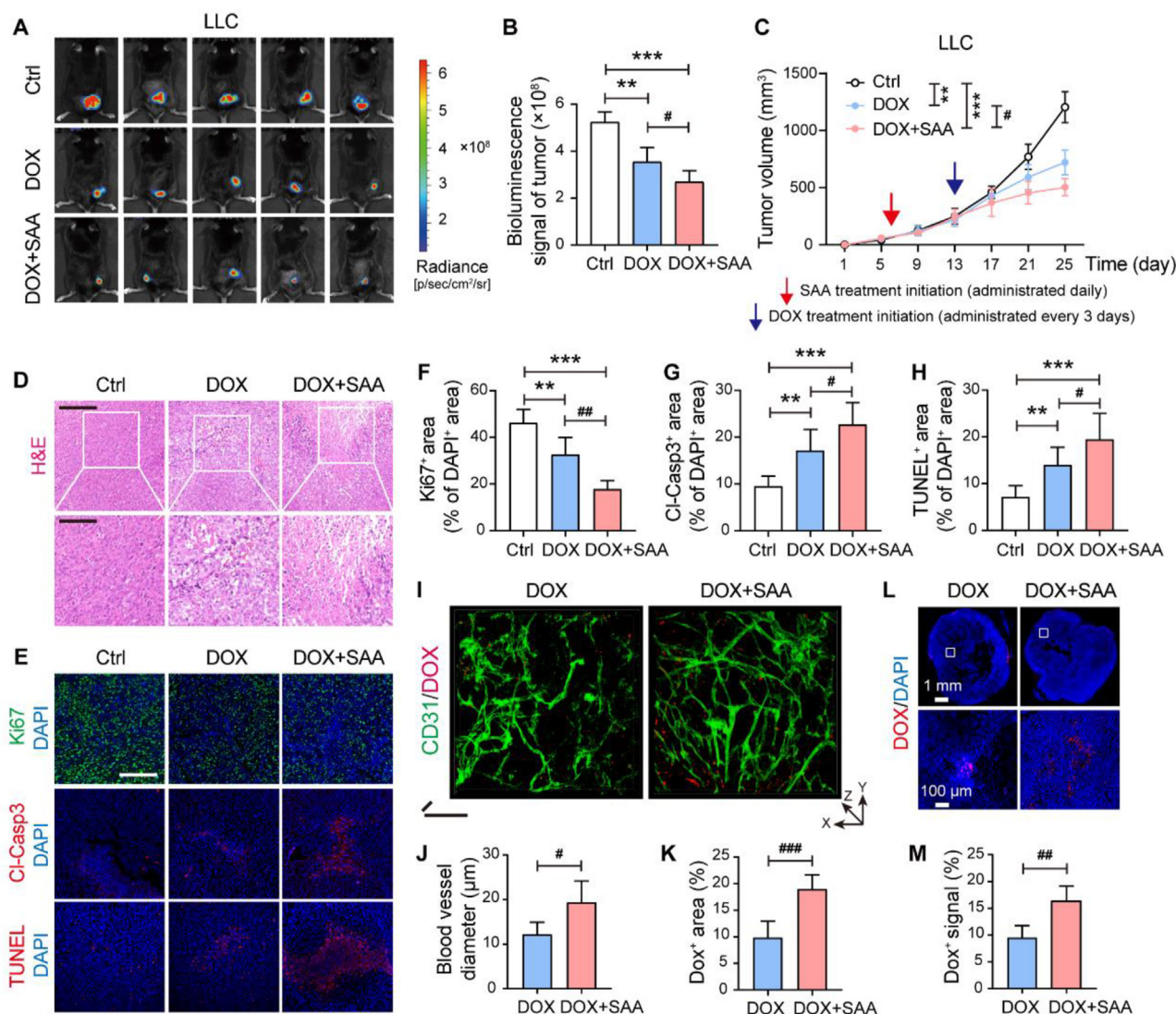
Figure 8 SAA propels the delivery of DOX into tumors and magnifies the anti-tumor effect. (A) *In vivo* bioluminescence images for LLC tumor bearing mice treated with Ctrl, DOX (8 mg/kg), and DOX + SAA ($n = 5$). (B) Quantification of bioluminescence signals in LLC tumors ($n = 5$). (C) The growth curves of LLC tumors ($n = 5$). The LLC tumor-bearing mice received saline or SAA treatment (daily administration) from day 6 and DOX treatment (administered every three days) from Day 13 following the subcutaneous inoculation of LLC tumor cells. (D) Representative H&E staining images in the LLC tumor-bearing mice. Scale bars: 200 μm (upper panel) and 100 μm (lower panel). (E) Representative immunofluorescence staining images for Ki67 (green), Cl-Casp3 (red), and TUNEL (red) in the LLC tumor-bearing mice. Scale bars: 200 μm. (F−H) Quantification for Ki67$^+$ cells (F), Cl-Casp3$^+$ cells (G), and TUNEL$^+$ cells (H) of DAPI$^+$ cells in the LLC tumors ($n = 5$). (I) *Ex vivo* two-photon microscopic images for CD31/DOX in the LLC tumors. Scale bars for *x* axis: 50 μm; scale bars for *z* axis: 50 μm. (J, K) Quantification for vessel diameter (J) and DOX$^+$ area (K) in the LLC tumors ($n = 5$). (L, M) Representative images for DOX distribution in the LLC tumors (L) and quantification for DOX$^+$ signals (M) ($n = 5$). Scale bars: 1 mm (upper panel) and 100 μm (lower panel). All data are presented as mean ± SD. Statistical analysis was performed using two-sided unpaired *t*-tests and ordinary one-way ANOVA. $^#P < 0.05$, $^{##}P < 0.01$, $^{###}P < 0.001$ *versus* DOX group. $^{**}P < 0.01$, $^{***}P < 0.001$ *versus* Ctrl group.

Nrf2[19,63,64]. The studies of PKM2 acting as a protein kinase highlight that, after translocation into the nucleus, PKM2 makes use of its metabolic substrate PEP as a phosphate donor for phosphorylation of a wealth of target proteins including Stat3, histone H3, MLC2, and ERK1/2[56,62,65,66]. In the present study, the direct connections between SAA and PKM2 offers an additional layer of modulation to endothelial metabolism and endothelial TJ. This connection emphasizes the roles of SAA in influencing endothelial behaviors beyond its contribution to hinder the pyruvate and lactate production in the ECs. These

regulated endothelial behaviors by SAA are more related to the strengthened endothelial integrity with increased expression of TJ-associated proteins. Other studies have also revealed that K433 of PKM2 and Y333 of β-Catenin play key roles in the interaction between PKM2 and β-Catenin, which subsequently influence cell biological behaviors[17]. The direct coupling of PKM2 with TJ in ECs *via* β-Catenin generates an intrinsic feedback loop to sense and respond to the changing energy[17]. Hence, it is illustrated that PKM2 participates in regulating the complex network of glycolysis and TJ, as well as has crucial

impacts on EC biological behaviors, implying that PKM2 may emerge as a promising target for reversing abnormal tumor blood vessels.

In this study, we unveiled the pharmacological effect of SAA in inducing tumor vascular normalization on the basis of a variety of *in vitro* and *in vivo* experiments. Additionally, we investigated the impacts of SAA on normal vascular structure, and it was revealed that SAA failed to influence the normal blood vessels. Although the specific effects of SAA on normal blood vessels still require further exploration, we do perceive that SAA is prone to exert its pharmacological effects on abnormal blood vessels that are present in tumor microenvironment. Considering the fact that normalized tumor blood vessels improve the delivery and distribution of the chemotherapeutic drugs into tumors[45,67], SAA was found to synergize with chemotherapeutic drug DOX for fighting against tumor progression. According to our data, SAA strikingly ameliorated the tumor hypoxic microenvironment rather than directly altered the apoptosis pattern to delay tumor progression. DOX as one of the anthracycline antibiotics has been widely used for cancer treatment. Nonetheless, the clinical usage of DOX appears to be limited owing to dose-dependent cardiotoxicity[68]. It has been reported that DOX potently yields nuclear chromatin condensation in the cardiomyocytes and thus reduction in body weight of tumor-bearing mice[69], which is consistent with our observation in this study. More importantly, we illustrated that SAA could profoundly alleviate various pathological phenotypes induced by DOX. Additionally, recent studies have also shown that SAA prominently diminishes the inflammation in the damaged heart caused by DOX[70,71], implying that SAA exerts striking therapeutic effect on DOX-induced cardiotoxicity. As such, SAA can synergize with DOX and reduce its potential toxicity in the treatment of tumors.

5. Conclusions

In conclusion, we demonstrated that inhibition of PKM2 tetramer in the ECs elicited tumor vascular normalization with alleviated hypoxia microenvironment. SAA was capable of altering endothelial glycolysis *via* directly binding to PKM2 and determining the fate of endothelial TJ by virtue of regulating β-Catenin/Claudin-5 signaling axis. More interestingly, it was observed that PKM2 expression in tumor endothelium of lung cancer patients was closely associated with tumor progression and differentiation, which could act as a potential biomarker for dissecting tumor vascular behaviors and appeared to be a novel target for anti-angiogenesis therapy. Additionally, relying on the function of normalizing tumor blood vessels, SAA reinforced the penetration and distribution of chemotherapy drug DOX in tumors, providing a novel strategy of combination therapy. Taken together, our findings offer novel insights into the pharmacological activities and mechanisms of SAA in retarding tumor progression.

Acknowledgments

Author contributions

Yang Zhao, Yin Lu, and Aiyun Wang conceived and led the project. Cheng Qian carried out most of the experiments and analyzed the data. Yueke Zhou, Teng Zhang, Guanglu Dong, Mengyao Song, Yu Tang, Zhonghong Wei, Suyun Yu, Qiuhong Shen, Chongjin Zhong, and Li Wan performed and analyzed parts of the experiments. Wenxing Chen, Jaesung P. Choi, Juming Yan, and Jia Li discussed the experimental studies, commented on, and proofread the manuscript. Yang Zhao and Cheng Qian wrote and revised the manuscript with input from all authors. All authors read and approved the final manuscript.

Conflict of interest

The authors declare that they have no known competing financial interests or personal relationships that could have appeared to influence the work reported in this paper.

Appendix A.   Supporting information

Supporting data to this article can be found online at https://doi.org/10.1016/j.apsb.2024.02.003.

References

1. Palikuqi B, Nguyen DT, Li G, Schreiner R, Pellegata AF, Liu Y, et al. Adaptable haemodynamic endothelial cells for organogenesis and tumorigenesis. *Nature* 2020;**585**:426−32.
2. Vanlandewijck M, He L, Mae MA, Andrae J, Ando K, Del Gaudio F, et al. A molecular atlas of cell types and zonation in the brain vasculature. *Nature* 2018;**554**:475−80.
3. Shaked Y. The pro-tumorigenic host response to cancer therapies. *Nat Rev Cancer* 2019;**19**:667−85.
4. Apte RS, Chen DS, Ferrara N. VEGF in signaling and disease: beyond discovery and development. *Cell* 2019;**176**:1248−64.
5. Goel S, Duda DG, Xu L, Munn LL, Boucher Y, Fukumura D, et al. Normalization of the vasculature for treatment of cancer and other diseases. *Physiol Rev* 2011;**91**:1071−121.
6. Zhang D, Li AM, Hu GH, Huang MG, Yang F, Zhang L, et al. PHGDH-mediated endothelial metabolism drives glioblastoma resistance to chimeric antigen receptor T cell immunotherapy. *Cell Metabol* 2023;**35**:517−34.
7. Qian C, Yang C, Tang Y, Zheng W, Zhou Y, Zhang S, et al. Pharmacological manipulation of Ezh2 with salvianolic acid B results in tumor vascular normalization and synergizes with cisplatin and T cell-mediated immunotherapy. *Pharmacol Res* 2022;**182**:106333.
8. Cao YH, Langer R, Ferrara N. Targeting angiogenesis in oncology, ophthalmology and beyond. *Nat Rev Drug Discov* 2023;**22**:476−95.
9. Kalucka J, de Rooij L, Goveia J, Rohlenova K, Dumas SJ, Meta E, et al. Single-cell transcriptome atlas of murine endothelial cells. *Cell* 2020;**180**:764−79.

10. Eelen G, de Zeeuw P, Treps L, Harjes U, Wong BW, Carmeliet P. Endothelial cell metabolism. *Physiol Rev* 2018;**98**:3−58.

11. Rohlenova K, Goveia J, Garcia-Caballero M, Subramanian A, Kalucka J, Treps L, et al. Single-cell RNA sequencing maps endothelial metabolic plasticity in pathological angiogenesis. *Cell Metabol* 2020;**31**:862−77.

12. Cantelmo AR, Conradi LC, Brajic A, Goveia J, Kalucka J, Pircher A, et al. Inhibition of the glycolytic activator PFKFB3 in endothelium induces tumor vessel normalization, impairs metastasis, and improves chemotherapy. *Cancer Cell* 2016;**30**:968−85.

13. Li X, Sun X, Carmeliet P. Hallmarks of endothelial cell metabolism in health and disease. *Cell Metabol* 2019;**30**:414−33.

14. Falkenberg KD, Rohlenova K, Luo Y, Carmeliet P. The metabolic engine of endothelial cells. *Nat Metab* 2019;**1**:937−46.

15. Cruys B, Wong BW, Kuchnio A, Verdegem D, Cantelmo AR, Conradi LC, et al. Glycolytic regulation of cell rearrangement in angiogenesis. *Nat Commun* 2016;**7**:12240.

16. Morita M, Sato T, Nomura M, Sakamoto Y, Inoue Y, Tanaka R, et al. PKM1 confers metabolic advantages and promotes cell-autonomous tumor cell growth. *Cancer Cell* 2018;**33**:355−67.

17. Yang W, Xia Y, Ji H, Zheng Y, Liang J, Huang W, et al. Nuclear PKM2 regulates beta-catenin transactivation upon EGFR activation. *Nature* 2011;**480**:118−22.

18. Saleme B, Gurtu V, Zhang Y, Kinnaird A, Boukouris AE, Gopal K, et al. Tissue-specific regulation of p53 by PKM2 is redox dependent and provides a therapeutic target for anthracycline-induced cardiotoxicity. *Sci Transl Med* 2019;**11**:eaau8866.

19. Wei Y, Lu M, Mei M, Wang H, Han Z, Chen M, et al. Pyridoxine induces glutathione synthesis *via* PKM2-mediated Nrf2 transactivation and confers neuroprotection. *Nat Commun* 2020;**11**:941.

20. Luo W, Hu H, Chang R, Zhong J, Knabel M, O'Meally R, et al. Pyruvate kinase M2 is a PHD3-stimulated coactivator for hypoxia-inducible factor 1. *Cell* 2011;**145**:732−44.

21. Kim B, Jang C, Dharaneeswaran H, Li J, Bhide M, Yang S, et al. Endothelial pyruvate kinase M2 maintains vascular integrity. *J Clin Invest* 2018;**128**:4543−56.

22. Siragusa M, Thole J, Bibli SI, Luck B, Loot AE, de Silva K, et al. Nitric oxide maintains endothelial redox homeostasis through PKM2 inhibition. *EMBO J* 2019;**38**:e100938.

23. Wu Y, Tang L, Huang H, Yu Q, Hu B, Wang G, et al. Phosphoglycerate dehydrogenase activates PKM2 to phosphorylate histone H3T11 and attenuate cellular senescence. *Nat Commun* 2023;**14**:1323.

24. Davies EM, Gurung R, Le KQ, Roan KTT, Harvey RP, Mitchell GM, et al. PI(4,5)P2-dependent regulation of endothelial tip cell specification contributes to angiogenesis. *Sci Adv* 2023;**9**: eadd6911.

25. Tang Y, Qian C, Zhou Y, Yu C, Song M, Zhang T, et al. Activated platelets facilitate hematogenous metastasis of breast cancer by modulating the PDGFR-beta/COX-2 axis. *iScience* 2023;**26**:107704.

26. Yang C, Qian C, Zheng W, Dong G, Zhang S, Wang F, et al. Ginsenoside Rh2 enhances immune surveillance of natural killer (NK) cells *via* inhibition of ERp5 in breast cancer. *Phytomedicine* 2023;**123**: 155180.

27. Chen X, Guo J, Bao J, Lu J, Wang Y. The anticancer properties of *Salvia miltiorrhiza* Bunge (Danshen): a systematic review. *Med Res Rev* 2014;**34**:768−94.

28. Song M, Qian C, Zhang T, Tang Y, Zhou Y, Wei Z, et al. *Salvia mitiorrhiza* Bunge aqueous extract attenuates infiltration of tumor-associated macrophages and potentiates anti-PD-L1 immunotherapy in colorectal cancer through modulating Cox2/PGE2 cascade. *J Ethnopharmacol* 2023;**316**:116735.

29. Zhao Y, Li J, Ting KK, Chen J, Coleman P, Liu K, et al. The VE-Cadherin/beta-catenin signalling axis regulates immune cell infiltration into tumours. *Cancer Lett* 2021;**496**:1−15.

30. Jing XM, Yang FM, Shao CC, Wei K, Xie MY, Shen H, et al. Role of hypoxia in cancer therapy by regulating the tumor microenvironment. *Mol Cancer* 2019;**18**:157.

31. Huang Y, Kim BYS, Chan CK, Hahn SM, Weissman IL, Jiang W. Improving immune−vascular crosstalk for cancer immunotherapy. *Nat Rev Immunol* 2018;**18**:195−203.

32. Zhong C, Jiang C, Ni S, Wang Q, Cheng L, Wang H, et al. Identification of bioactive anti-angiogenic components targeting tumor endothelial cells in Shenmai injection using multidimensional pharmacokinetics. *Acta Pharm Sin B* 2020;**10**:1694−708.

33. Bianco S, Mancardi D, Merlino A, Bussolati B, Munaron L. Hypoxia and hydrogen sulfide differentially affect normal and tumor-derived vascular endothelium. *Redox Biol* 2017;**12**:499−504.

34. McGarry T, Biniecka M, Veale DJ, Fearon U. Hypoxia, oxidative stress and inflammation. *Free Radic Biol Med* 2018;**125**:15−24.

35. Kim YW, Byzova TV. Oxidative stress in angiogenesis and vascular disease. *Blood* 2014;**123**:625−31.

36. Yamamoto M, Kensler TW, Motohashi H. The KEAP1−NRF2 system: a thiol-based sensor-effector apparatus for maintaining redox homeostasis. *Physiol Rev* 2018;**98**:1169−203.

37. Wong BW, Marsch E, Treps L, Baes M, Carmeliet P. Endothelial cell metabolism in health and disease: impact of hypoxia. *EMBO J* 2017; **36**:2187−203.

38. Lomenick B, Hao R, Jonai N, Chin RM, Aghajan M, Warburton S, et al. Target identification using drug affinity responsive target stability (DARTS). *Proc Natl Acad Sci U S A* 2009;**106**:21984−9.

39. Zhu YY, Ouyang ZJ, Du HJ, Wang MJ, Wang JJ, Sun HY, et al. New opportunities and challenges of natural products research: when target identification meets single-cell multiomics. *Acta Pharm Sin B* 2022; **12**:4011−39.

40. Zhang Z, Deng X, Liu Y, Liu Y, Sun L, Chen F. PKM2, function and expression and regulation. *Cell Biosci* 2019;**9**:52.

41. Tran KA, Zhang X, Predescu D, Huang X, Machado RF, Gothert JR, et al. Endothelial beta-catenin signaling is required for maintaining adult blood−brain barrier integrity and central nervous system homeostasis. *Circulation* 2016;**133**:177−86.

42. Taddei A, Giampietro C, Conti A, Orsenigo F, Breviario F, Pirazzoli V, et al. Endothelial adherens junctions control tight junctions by VE-cadherin-mediated upregulation of claudin-5. *Nat Cell Biol* 2008;**10**: 923−34.

43. Katoh M, Katoh M. WNT signaling and cancer stemness. *Essays Biochem* 2022;**66**:319−31.

44. Maes H, Kuchnio A, Peric A, Moens S, Nys K, De Bock K, et al. Tumor vessel normalization by chloroquine independent of autophagy. *Cancer Cell* 2014;**26**:190−206.

45. Sun Y, Chen W, Torphy RJ, Yao S, Zhu G, Lin R, et al. Blockade of the CD93 pathway normalizes tumor vasculature to facilitate drug delivery and immunotherapy. *Sci Transl Med* 2021;**13**:eabc8922.

46. Paskeh MDA, Saebfar H, Mahabady MK, Orouei S, Hushmandi K, Entezari M, et al. Overcoming doxorubicin resistance in cancer: siRNA-loaded nanoarchitectures for cancer gene therapy. *Life Sci* 2022;**298**:120463.

47. Lu D, Chatterjee S, Xiao K, Riedel I, Huang CK, Costa A, et al. A circular RNA derived from the insulin receptor locus protects against doxorubicin-induced cardiotoxicity. *Eur Heart J* 2022;**43**:4496−511.

48. Yang C, Qian C, Zhang T, Zheng W, Zhang S, Wang S, et al. The killing effect of tanshinol on breast cancer cells: insight into the reversion of TGF-beta1-mediated suppression of NK cell functions. *Front Biosci (Landmark Ed)* 2021;**26**:1106−18.

49. Vander Heiden MG, DeBerardinis RJ. Understanding the intersections between metabolism and cancer biology. *Cell* 2017;**168**:657−69.

50. Shan Y, Ni Q, Zhang Q, Zhang M, Wei B, Cheng L, et al. Targeting tumor endothelial hyperglycolysis enhances immunotherapy through remodeling tumor microenvironment. *Acta Pharm Sin B* 2022;**12**: 1825−39.

51. De Bock K, Georgiadou M, Carmeliet P. Role of endothelial cell metabolism in vessel sprouting. *Cell Metabol* 2013;**18**:634−47.

52. Kierans SJ, Taylor CT. Regulation of glycolysis by the hypoxia-inducible factor (HIF): implications for cellular physiology. *J Physiol* 2021;**599**:23−37.

53. McDonald PC, Chafe SC, Brown WS, Saberi S, Swayampakula M, Venkateswaran G, et al. Regulation of pH by carbonic anhydrase 9 mediates survival of pancreatic cancer cells with activated KRAS in response to hypoxia. *Gastroenterology* 2019;**157**:823−37.

54. Zhang Q, Liu J, Duan H, Li R, Peng W, Wu C. Activation of Nrf2/HO-1 signaling: an important molecular mechanism of herbal medicine in the treatment of atherosclerosis *via* the protection of vascular endothelial cells from oxidative stress. *J Adv Res* 2021;**34**:43−63.

55. Paik JY, Jung KH, Lee JH, Park JW, Lee KH. Reactive oxygen species-driven HIF1alpha triggers accelerated glycolysis in endothelial cells exposed to low oxygen tension. *Nucl Med Biol* 2017;**45**:8−14.

56. Damasceno LEA, Prado DS, Veras FP, Fonseca MM, Toller-Kawahisa JE, Rosa MH, et al. PKM2 promotes Th17 cell differentiation and autoimmune inflammation by fine-tuning STAT3 activation. *J Exp Med* 2020;**217**:e20190613.

57. Dayton TL, Jacks T, Vander Heiden MG. PKM2, cancer metabolism, and the road ahead. *EMBO Rep* 2016;**17**:1721−30.

58. Hitosugi T, Kang S, Vander Heiden MG, Chung TW, Elf S, Lythgoe K, et al. Tyrosine phosphorylation inhibits PKM2 to promote the Warburg effect and tumor growth. *Sci Signal* 2009;**2**:ra73.

59. Lv L, Li D, Zhao D, Lin R, Chu Y, Zhang H, et al. Acetylation targets the M2 isoform of pyruvate kinase for degradation through chaperone-mediated autophagy and promotes tumor growth. *Mol Cell* 2011;**42**:719−30.

60. Anastasiou D, Poulogiannis G, Asara JM, Boxer MB, Jiang JK, Shen M, et al. Inhibition of pyruvate kinase M2 by reactive oxygen species contributes to cellular antioxidant responses. *Science* 2011;**334**:1278−83.

61. Christofk HR, Vander Heiden MG, Harris MH, Ramanathan A, Gerszten RE, Wei R, et al. The M2 splice isoform of pyruvate kinase is important for cancer metabolism and tumour growth. *Nature* 2008;**452**:230−3.

62. Jiang Y, Wang Y, Wang T, Hawke DH, Zheng Y, Li X, et al. PKM2 phosphorylates MLC2 and regulates cytokinesis of tumour cells. *Nat Commun* 2014;**5**:5566.

63. Azoitei N, Becher A, Steinestel K, Rouhi A, Diepold K, Genze F, et al. PKM2 promotes tumor angiogenesis by regulating HIF-1alpha through NF-kappaB activation. *Mol Cancer* 2016;**15**:3.

64. Palsson-McDermott EM, Curtis AM, Goel G, Lauterbach MA, Sheedy FJ, Gleeson LE, et al. Pyruvate kinase M2 regulates Hif-1alpha activity and IL-1beta induction and is a critical determinant of the warburg effect in LPS-activated macrophages. *Cell Metabol* 2015;**21**:65−80.

65. Yang W, Xia Y, Hawke D, Li X, Liang J, Xing D, et al. PKM2 phosphorylates histone H3 and promotes gene transcription and tumorigenesis. *Cell* 2012;**150**:685−96.

66. Yang W, Zheng Y, Xia Y, Ji H, Chen X, Guo F, et al. ERK1/2-dependent phosphorylation and nuclear translocation of PKM2 promotes the Warburg effect. *Nat Cell Biol* 2012;**14**:1295−304.

67. Xu Z, Guo C, Ye Q, Shi Y, Sun Y, Zhang J, et al. Endothelial deletion of SHP2 suppresses tumor angiogenesis and promotes vascular normalization. *Nat Commun* 2021;**12**:6310.

68. Burridge PW, Li YF, Matsa E, Wu H, Ong SG, Sharma A, et al. Human induced pluripotent stem cell-derived cardiomyocytes recapitulate the predilection of breast cancer patients to doxorubicin-induced cardiotoxicity. *Nat Med* 2016;**22**:547−56.

69. Shi J, Li J, Li J, Li R, Wu X, Gao F, et al. Synergistic breast cancer suppression efficacy of doxorubicin by combination with glycyrrhetinic acid as an angiogenesis inhibitor. *Phytomedicine* 2021;**81**:153408.

70. Qi JY, Yang YK, Jiang C, Zhao Y, Wu YC, Han X, et al. Exploring the mechanism of danshensu in the treatment of doxorubicin-induced cardiotoxicity based on network pharmacology and experimental evaluation. *Front Cardiovasc Med* 2022;**9**:827975.

71. Yi X, Wang F, Feng Y, Zhu J, Wu Y. Danhong injection attenuates doxorubicin-induced cardiotoxicity in rats *via* suppression of apoptosis: network pharmacology analysis and experimental validation. *Front Pharmacol* 2022;**13**:929302.